PHYSICAL REVIEW D **72,** 034032 (2005)

Next-to-leading order QCD predictions for A^0Z^0 associated production at the CERN Large Hadron Collider

Qiang Li, Chong Sheng Li,* and Jian Jun Liu
Department of Physics, Peking University, Beijing 100871, China

Li Gang Jin
Institute of Theoretical Physics, Academia Sinica, Beijing 100080, China

C.-P. Yuan†
Department of Physics and Astronomy, Michigan State University, East Lansing, Michigan 48824, USA
(Received 27 March 2005; revised manuscript received 18 July 2005; published 30 August 2005)

We present the calculations of the complete next-to-leading order (NLO) QCD corrections (including supersymmetric QCD) to the inclusive total cross sections of the associated production processes $pp \to A^0Z^0 + X$ in the minimal supersymmetric standard model at the CERN Large Hadron Collider. Both the dimensional regularization scheme and the dimensional reduction scheme are used to organize the calculations, which yield the same NLO rates. The NLO correction can either enhance or reduce the total cross sections, but it generally efficiently reduces the dependence of the total cross sections on the renormalization/factorization scale. We also examine the uncertainty of the total cross sections due to the parton distribution function uncertainties.

DOI: 10.1103/PhysRevD.72.034032 PACS numbers: 12.38.Bx, 12.60.Jv, 14.70.Hp, 14.80.Cp

I. INTRODUCTION

The search for one or more Higgs bosons is the central task of the CERN Large Hadron Collider (LHC), with $\sqrt{S} = 14$ TeV and a luminosity of 100 fb^{-1} per year. In the standard model (SM), the Higgs boson mass is a free parameter with an upper bound of $m_H \leq 600$–800 GeV [1]. Beyond the SM, the minimal supersymmetric standard model (MSSM), whose Higgs sector is a special case of the two Higgs doublet model (2HDM) [2], is of particular theoretical interest, and contains five physical Higgs bosons: two neutral CP-even bosons h^0 and H^0, one neutral CP-odd boson A^0, and two charged bosons $H^{\pm}$. The h^0 is the lightest, with a mass $m_{h^0} \leq 140$ GeV when including the radiative corrections [3], and is a SM-like Higgs boson especially in the decoupling region ($m_{A^0} \gg m_{Z^0}$). The other four are non-SM-like ones, and the discovery of them may give the direct evidence of the MSSM. It has been shown in Refs. [4,5] that the h^0 boson of MSSM cannot escape detection at the CERN LHC and that more than one neutral Higgs particle can be found in a large area of the supersymmetry (SUSY) parameter space

At the LHC, the neutral Higgs bosons can be produced through the following mechanisms: gluon fusion $gg \to \phi$ [6–9], weak boson fusion $qq \to qqV^*V^* \to qqh^0/qqH^0$ [10], associated production with weak bosons [11–13], associated production with a heavy quark-antiquark pair $gg, q\bar{q} \to t\bar{t}\phi/b\bar{b}\phi$ [14], and pairs production [15]. Studying the associated production process of a neutral Higgs boson and a vector boson at future hadron colliders may be an interesting way to search for neutral Higgs bosons, since the total cross section may be large and also the leptonic decay of the vector boson can be used as a spectacular event trigger. In the SM, the process $q\bar{q}^{(\prime)} \to W/Z^0h^0_{\text{SM}}$ has been studied both at the leading order (LO) [11] and the next-to-leading order (NLO) [13,16] in QCD. In the 2HDM and MSSM, the associated production of $h^0(H^0)Z^0$ and A^0Z^0 has been studied only at tree level for the Drell-Yan process and at one-loop level for gluon fusion in Refs. [17–20], respectively.

It was shown in Ref. [18] that the A^0Z^0 associated production rate at the LHC strongly depends on the SUSY parameters $\tan\beta$ (the ratio of two vacuum expectation values) and m_A (the mass of A^0). The total cross section increases with an increment of $\tan\beta$ and decreases with an increment of m_A. In this paper, we present the complete NLO QCD, including supersymmetric QCD, calculation for the cross section of the associated production of A^0Z^0 through the $b\bar{b}$ annihilation process at the LHC. For simplicity, in our calculation, we neglect the bottom quark mass except in the Yukawa couplings. Such approximations are valid in all diagrams, in which the bottom quark appears as an initial state parton, according to the simplified Aivazis-Collins-Olness-Tung scheme [21]. To regularize the ultraviolet (UV), soft, and collinear divergences, two regularization schemes are used in our calculations for a cross check, i.e. the dimensional regularization (DREG) scheme [22] (with the naive γ_5 scheme [23]) and the dimensional reduction (DRED) scheme [24], and their results are compared.

The arrangement of this paper is as follows. In Sec. II, we show the LO results and define the notations. In Sec. III, we present the details of the calculations of both the virtual

*Electronic address: csli@pku.edu.cn
†Electronic address: yuan@pa.msu.edu

and the real parts of the NLO QCD corrections and compare the results in DREG with those in DRED. In Sec. IV, by a detailed numerical analysis, we present the predictions for the inclusive and the differential cross sections of the A^0Z^0 associated production at the LHC. Section V contains a brief conclusion. For completeness, the relevant Feynman rules are collected in Appendix A, and the lengthy analytic expressions of the result of our calculation are summarized in Appendix B.

II. LEADING ORDER CALCULATIONS

The related Feynman diagrams which contribute to the LO amplitude of the partonic process $b(p_1)\bar{b}(p_2) \to Z^0(p_3)A^0(p_4)$ are shown in Fig. 1. The LO amplitude in $n = 4 - 2\epsilon$ dimensions is

$$M^B = \delta_{i_1 i_2}\mu_r^{4-n}[M_0^{(s)} + M_0^{(t)} + M_0^{(u)}],$$

with

$$M_0^{(s)} = 2im_b\left(\frac{A_1F_1}{s-m_{h^0}^2} + \frac{A_2F_2}{s-m_{H^0}^2}\right)\overline{v}(p_2)u(p_1)p_4\cdot\varepsilon_\rho(p_3),$$

$$M_0^{(t)} = \frac{im_bA_3}{t}\overline{v}(p_2)\gamma^5(\not{p}_1 - \not{p}_3)\not{\varepsilon}(p_3)(C_V + C_A\gamma^5)u(p_1),$$

$$M_0^{(u)} = \frac{im_bA_3}{u}\overline{v}(p_2)\not{\varepsilon}(p_3)(C_V + C_A\gamma^5)(\not{p}_1 - \not{p}_4)\gamma^5u(p_1),$$

where $\delta_{i_1 i_2}$ is the color tensor (i_1, i_2 are color indices for the initial state quarks), μ_r is a mass parameter introduced to keep the couplings dimensionless, s, t, and u are Mandelstam variables, which are defined as

$$s = (p_1 + p_2)^2, \quad t = (p_1 - p_3)^2, \quad u = (p_2 - p_3)^2,$$

$A_{i=1,2,3}$, $F_{i=1,2}$, and $C_{V,A}$ denote the coefficients appearing in the relevant $h^0(H^0, A^0)b\bar{b}$, $h^0(H^0)Z^0A^0$, and $Z^0b\bar{b}$ couplings, respectively, and their explicit expressions are given in Appendix A.

In order to simplify the expressions, we further introduce the following Mandelstam variables:

$$t' = t - m_{Z^0}^2, \qquad u' = u - m_{Z^0}^2. \tag{1}$$

After the n-dimensional phase space integration, the LO partonic differential cross sections are given by

$$\frac{d^2\hat{\sigma}^B}{dt'du'} = \frac{\pi S_\epsilon}{s^2\Gamma(1-\epsilon)}\left(\frac{t'u' - sm_{Z^0}^2}{\mu_r^2 s}\right)^{-\epsilon}\Theta(t'u' - sm_{Z^0}^2) \times \Theta[s - (m_{Z^0} + m_{A^0})^2]\delta(s + t + u - m_{Z^0}^2 - m_{A^0}^2)\overline{\sum}|M^B|^2, \tag{2}$$

with

$$\begin{aligned}\overline{\sum}|M^B|^2 = \frac{m_b^2}{6}\Bigg\{&\left[4m_{A^0}^2 s - \frac{(s - m_{Z^0}^2 - m_{A^0}^2)^2 s}{m_{Z^0}^2}\right]\left(\frac{A_1F_1}{s-m_{h^0}^2} + \frac{A_2F_2}{s-m_{H^0}^2}\right)^2 + A_3^2(|C_V|^2 + |C_A|^2) \\ &\times \frac{2m_{Z^0}^2(1-\epsilon)(tu - m_{Z^0}^2m_{A^0}^2) + st^2}{m_{Z^0}^2t^2} + A_3^2(|C_V|^2 + |C_A|^2)\frac{2m_{Z^0}^2(1-\epsilon)(tu - m_{Z^0}^2m_{A^0}^2) + su^2}{m_{Z^0}^2u^2} \\ &+ \frac{4A_3C_As(t+u)(tu - m_{Z^0}^2m_{A^0}^2)}{tum_{Z^0}^2}\left[\frac{A_1F_1}{(s-m_{h^0}^2)} + \frac{A_2F_2}{(s-m_{H^0}^2)}\right] + 2A_3^2(|C_V|^2 - |C_A|^2) \\ &\times \frac{2(1-\epsilon)m_{Z^0}^2(tu - m_{Z^0}^2m_{A^0}^2) + s(2m_{Z^0}^2m_{A^0}^2 - tu)}{m_{Z^0}^2tu}\Bigg\},\end{aligned} \tag{3}$$

where $S_\epsilon = (4\pi)^{-2+\epsilon}$ and the Θ function is the Heaviside step function. $\overline{\sum}|M^B|^2$ is the LO squared matrix element of $b(x_1p_1)\bar{b}(x_2p_2) \to Z^0(p_3)A^0(p_4)$, in which the colors and the spins of the outgoing particles have been summed, and the colors and the spins of the incoming ones have been averaged over.

The LO total cross section at the LHC is obtained by convoluting the partonic cross section with the parton distribution functions (PDFs) $G_{b,\bar{b}/p}$ in the proton:

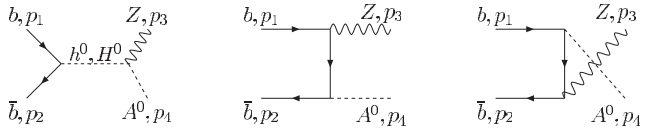

FIG. 1. Leading order Feynman diagrams for $b\bar{b} \to A^0Z^0$.

$$\sigma^B = \int dx_1dx_2[G_{b/p}(x_1,\mu_f)G_{\bar{b}/p}(x_2,\mu_f) + (x_1 \leftrightarrow x_2)]\hat{\sigma}^B, \tag{4}$$

where μ_f is the factorization scale and $\hat{\sigma}^B$ is the Born level constituent cross section of $b(x_1p_1)\bar{b}(x_2p_2) \to Z^0(p_3)A^0(p_4)$. Obviously, the above LO results in the DREG scheme are equal to the ones in the DRED scheme since the LO calculations are finite and free of any singularity.

III. NEXT-TO-LEADING ORDER CALCULATIONS

The NLO contributions to the associated production of A^0 and Z^0 can be separated into the virtual corrections arising from loop diagrams of colored particles and the real corrections arising from the radiation of a real gluon or a massless (anti)quark. For both the virtual and the real corrections, we will first present the results in the DREG scheme and then compare them with the ones obtained in the DRED scheme.

A. Virtual corrections

The virtual corrections to $b\bar{b} \to A^0 Z^0$ arise from the Feynman diagrams shown in Figs. 2 and 3. They consist of self-energy, vertex, and box diagrams, which represent the SM QCD corrections, arising from quarks and gluons, and supersymmetric QCD corrections, arising from squarks and gluinos. We carried out the calculation in the 't Hooft-Feynman gauge and used the dimensional regularization in $n = 4 - 2\epsilon$ dimensions to regularize the UV, soft, and collinear divergences in the virtual loop corrections. In order to remove the UV divergences, we renormalize the bottom quark masses in the Yukawa couplings and the wave function of the bottom quark, adopting the on-shell renormalization scheme [25].

Denoting m_{b0} and ψ_{b0} as the bare bottom quark mass and the bare wave function, respectively, the relevant renormalization constants δm_b, δZ_{bL}, and δZ_{bR} are then defined as

$$m_{b0} = m_b + \delta m_b, \tag{5}$$

$$\psi_{b0} = (1 + \delta Z_{bL})^{1/2} \psi_{bL} + (1 + \delta Z_{bR})^{1/2} \psi_{bR}. \tag{6}$$

After calculating the self-energy diagrams in Fig. 2, we obtain the explicit expressions of all the renormalization constants as follows:

$$\frac{\delta m_b}{m_b} = -\frac{\alpha_s}{4\pi} C_F \Big\{ 3B_0(m_b^2, 0, m_b^2) - 2 + \sum_{i=1}^{2} \Big[B_1 - \frac{m_{\tilde{g}}}{m_b} \times \sin 2\theta_{\tilde{b}} (-1)^i B_0 \Big] (m_b^2, m_{\tilde{g}}^2, m_{\tilde{b}_i}^2) \Big\},$$

$$\delta Z_{bL} = -\frac{\alpha_s}{2\pi} C_F \sum_{i=1}^{2} (R_{i1}^{\tilde{b}})^2 (B_0 + B_1)(0, m_{\tilde{b}_i}^2, m_{\tilde{g}}^2),$$

$$\delta Z_{bR} = -\frac{\alpha_s}{2\pi} C_F \sum_{i=1}^{2} (R_{i2}^{\tilde{b}})^2 (B_0 + B_1)(0, m_{\tilde{b}_i}^2, m_{\tilde{g}}^2),$$

where $C_F = \frac{4}{3}$, B_0, B_1 are the scalar two-point integrals [26], $m_{\tilde{b}_{1,2}}$ are the sbottom masses, $m_{\tilde{g}}$ is the gluino mass, and $R^{\tilde{b}}$ is a 2×2 matrix shown as below, which is defined to transform the sbottom current eigenstates to the mass eigenstates [27]:

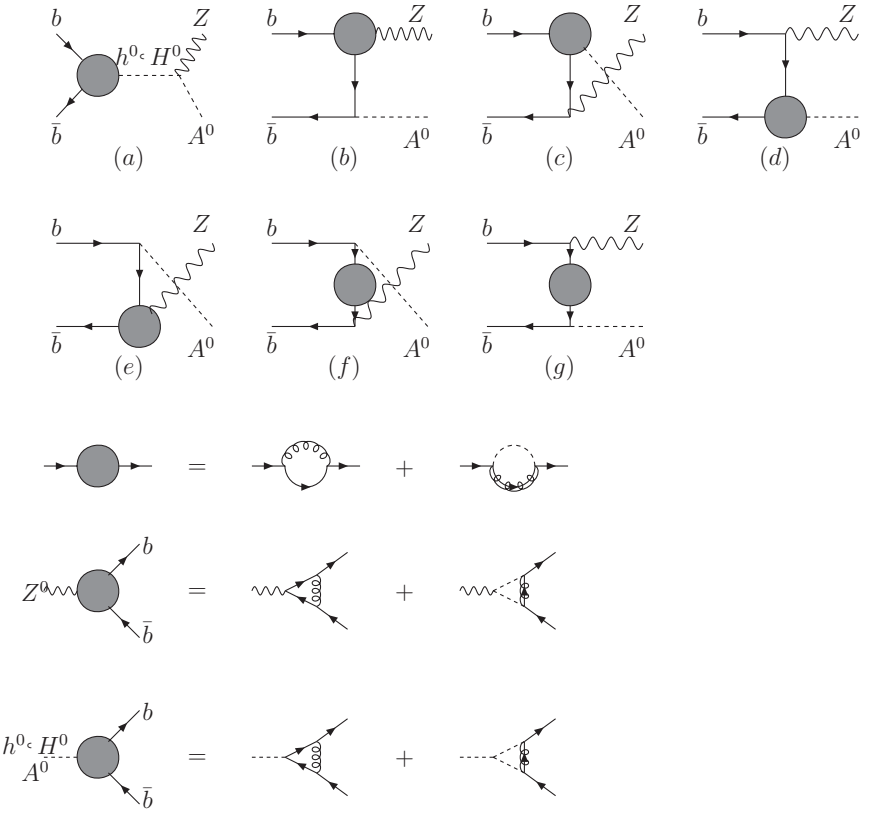

FIG. 2. One-loop virtual diagrams, including self-energy and vertex corrections for $b\bar{b} \to A^0 Z^0$.

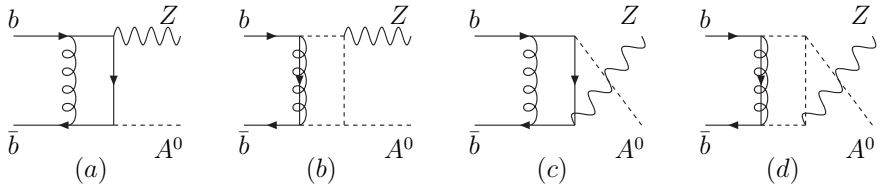

FIG. 3. Box diagrams for $b\bar{b} \to A^0 Z^0$.

$$\begin{pmatrix} \tilde{b}_1 \\ \tilde{b}_2 \end{pmatrix} = R^{\tilde{b}} \begin{pmatrix} \tilde{b}_L \\ \tilde{b}_R \end{pmatrix}, \qquad R^{\tilde{b}} = \begin{pmatrix} \cos\theta_{\tilde{b}} & \sin\theta_{\tilde{b}} \\ -\sin\theta_{\tilde{b}} & \cos\theta_{\tilde{b}} \end{pmatrix}, \quad (7)$$

with $0 \le \theta_{\tilde{b}} < \pi$, by convention. Correspondingly, the mass eigenvalues $m_{\tilde{b}_1}$ and $m_{\tilde{b}_2}$ (with $m_{\tilde{b}_1} \le m_{\tilde{b}_2}$) are given by

$$\begin{pmatrix} m^2_{\tilde{b}_1} & 0 \\ 0 & m^2_{\tilde{b}_2} \end{pmatrix} = R^{\tilde{b}} M^2_{\tilde{b}} (R^{\tilde{b}})^\dagger, \qquad M^2_{\tilde{b}} = \begin{pmatrix} m^2_{\tilde{b}_L} & a_b m_b \\ a_b m_b & m^2_{\tilde{b}_R} \end{pmatrix}, \quad (8)$$

with

$$m^2_{\tilde{b}_L} = M^2_{\tilde{Q}} + m^2_b + m^2_Z \cos 2\beta (I^b_{3L} - e_b \sin^2\theta_W), \quad (9)$$

$$m^2_{\tilde{b}_R} = M^2_{\tilde{D}} + m^2_b + m^2_Z \cos 2\beta e_b \sin^2\theta_W, \quad (10)$$

$$a_b = A_b - \mu \tan\beta. \quad (11)$$

Here $M^2_{\tilde{b}}$ is the sbottom mass matrix. $M_{\tilde{Q},\tilde{D}}$ and A_b are soft SUSY breaking parameters and μ is the Higgsino mass parameter . I^b_{3L} and e_b are the third component of the weak isospin (i.e. $-1/2$) and the electric charge of the bottom quark b (i.e. $-1/3$), respectively.

The renormalized virtual amplitudes can be written as

$$M^V = M^{\text{unren}} + M^{\text{con}}. \quad (12)$$

Here M^{unren} contains the radiative corrections from the one-loop self-energy, vertex, and box diagrams, as shown in Fig. 2, and M^{con} is the corresponding counterterm. Moreover, M^{unren} can be separated into two parts:

$$M^{\text{unren}} = \sum_{\alpha=a}^{g} M^\alpha + \sum_{\beta=a}^{d} M^{\text{box}(\beta)}, \quad (13)$$

where α and β denote the corresponding diagram indexes in Figs. 2 and 3, respectively. They can be further expressed as

$$M^\alpha = \sum_{l=1}^{12} f^\alpha_l M_l, \quad (14)$$

$$M^{\text{box}(\beta)} = \sum_{l=1}^{12} f^{\text{box}(\beta)}_l M_l, \quad (15)$$

$$M^{\text{unren}} = \sum_{l=1}^{12} f^{\text{unren}}_l M_l, \qquad (f^{\text{unren}}_l = f^\alpha_l + f^{\text{box}(\beta)}_l), \quad (16)$$

where f^α_l and $f^{\text{box}(\beta)}_l$ are the form factors, which are given explicitly in Appendix B, and the M_l are the standard matrix elements defined as

$$\begin{aligned} M_{1(2)} &= \bar{v}(p_2)u(p_1)p_{1(2)}\cdot\epsilon(p_3), \\ M_{3(4)} &= \bar{v}(p_2)P_R u(p_1)p_{1(2)}\cdot\epsilon(p_3), \\ M_5 &= \bar{v}(p_2)\not{p}_3\not{\epsilon}(p_3)u(p_1), \\ M_6 &= \bar{v}(p_2)\not{p}_3\not{\epsilon}(p_3)P_R u(p_1), \\ M_{7(8)} &= \bar{v}(p_2)\not{p}_3 P_R u(p_1)p_{1(2)}\cdot\epsilon(p_3), \\ M_9 &= \bar{v}(p_2)\not{\epsilon}(p_3)u(p_1), \\ M_{10} &= \bar{v}(p_2)\not{\epsilon}(p_3)P_R u(p_1), \\ M_{11(12)} &= \bar{v}(p_2)\not{p}_3 u(p_1)p_{1(2)}\cdot\epsilon(p_3). \end{aligned} \quad (17)$$

The counterterm contribution M^{con} is separated into $M^{\text{con}(s)}$, $M^{\text{con}(t)}$, and $M^{\text{con}(u)}$, i.e. the counterterms for s, t, and u channels, respectively, which are given by

$$M^{\text{con}} = M^{\text{con}(s)} + M^{\text{con}(t)} + M^{\text{con}(u)}, \qquad M^{\text{con}(s)} = 2i\left(\frac{A_1 F_1}{s - m^2_{h^0}} + \frac{A_2 F_2}{s - m^2_{H^0}}\right)\left[\delta m_b + \frac{m_b}{2}(\delta Z_{bL} + \delta Z_{bR})\right](M_1 + M_2),$$

$$M^{\text{con}(t)} = \frac{-iA_3}{t}\left[\delta m_b + \frac{m_b}{2}(\delta Z_{bL} + \delta Z_{bR})\right][2(C_V - C_A)M_1 - 4C_V M_3 - (C_V - C_A)M_5 + 2C_V M_6],$$

$$M^{\text{con}(u)} = \frac{iA_3}{u}\left[\delta m_b + \frac{m_b}{2}(\delta Z_{bL} + \delta Z_{bR})\right][2(C_V + C_A)M_2 - 4C_V M_4 + (C_V + C_A)M_5 - 2C_V M_6].$$

The $\mathcal{O}(\alpha_s)$ virtual corrections to the differential cross section can be expressed as

$$\frac{d^2\hat{\sigma}^V}{dt'du'} = \frac{\pi S_\epsilon}{s^2\Gamma(1-\epsilon)}\left(\frac{t'u' - sm_{Z^0}^2}{\mu_r^2 s}\right)^{-\epsilon}\Theta(t'u' - sm_{Z^0}^2) \times \Theta[s - (m_{Z^0} + m_{A^0})^2]\delta(s + t + u - m_{A^0}^2 - m_{Z^0}^2)2\,\mathrm{Re}\left[\overline{\sum}(M^V M^{B*})\right], \quad (18)$$

where the renormalized amplitude M^V is UV finite, but it still contains the infrared (IR) divergences:

$$M^V|_{\mathrm{IR}} = \frac{\alpha_s}{2\pi}\frac{\Gamma(1-\epsilon)}{\Gamma(1-2\epsilon)}\left(\frac{4\pi\mu_r^2}{s}\right)^{\epsilon}\left(\frac{A_2^V}{\epsilon^2} + \frac{A_1^V}{\epsilon}\right)M^B, \quad (19)$$

where

$$A_2^V = -C_F, \qquad A_1^V = -\tfrac{3}{2}C_F. \quad (20)$$

Here the infrared divergences include the soft divergences and the collinear divergences. The soft divergences are cancelled after adding the real emission corrections, and the remaining collinear divergences can be absorbed into the redefinition of PDF [28], which will be discussed in the following subsections. Note that the coefficients A_2^V and A_1^V of the infrared divergence terms are constants, similar to the Drell-Yan type processes. Needless to say that the SUSY-QCD corrections do not generate infrared divergences, for squarks and gluinos are massive particles.

In the above calculation, we have adopted the naive γ_5 prescription in the DREG scheme to calculate the A^0Z^0 associated production rate. To cross-check the above calculation, we shall also adopt the DRED scheme to carefully treat the γ_5 factor in the amplitude calculation. We shall show that the total inclusive rate is independent of the regularization scheme, though the individual contributions, from either virtual or real emission corrections, can be scheme-dependent.

In the DRED scheme, δZ_{bL} and δZ_{bR} remain unchanged; however, δm_b is different, and

$$\left(\frac{\delta m_b}{m_b}\right)_{\mathrm{DREG}} - \left(\frac{\delta m_b}{m_b}\right)_{\mathrm{DRED}} = \frac{\alpha_s}{4\pi}C_F. \quad (21)$$

Similarly, the form factors are found to be different, and

$$f_i^{\mathrm{unren}}{}_{\mathrm{DREG}} - f_i^{\mathrm{unren}}{}_{\mathrm{DRED}} = -\frac{\alpha_s}{2\pi}C_F \quad \text{for } i = 1, 2 \ldots 6, \quad (22)$$

$$f_i^{\mathrm{unren}}{}_{\mathrm{DREG}} - f_i^{\mathrm{unren}}{}_{\mathrm{DRED}} = 0 \quad \text{for } i = 7, 8 \ldots 12. \quad (23)$$

Thus, it is easy to obtain the following relations from the above results:

$$M^V{}_{\mathrm{DREG}} - M^V{}_{\mathrm{DRED}} = -\frac{\alpha_s}{4\pi}C_F M^B, \quad (24)$$

$$\sigma^V{}_{\mathrm{DREG}} - \sigma^V{}_{\mathrm{DRED}} = -\frac{\alpha_s}{2\pi}C_F\sigma^B + \mathcal{O}(\alpha_s^2). \quad (25)$$

B. Real gluon emission

The Feynman diagrams for the real gluon emission process $b(p_1)\bar{b}(p_2) \to Z^0(p_3)A^0(p_4) + g(p_5)$ are shown in Fig. 4.

The phase space integration for the real gluon emission will produce infrared singularities, which can be either soft or collinear and can be conveniently isolated by slicing the phase space into different regions defined by suitable cutoffs. In this paper, we use the two-cutoff phase space slicing method [29], which introduces two small cutoffs to decompose the three-body phase space into three regions.

First, the phase space can be separated into two regions by an arbitrary small soft cutoff δ_s, according to whether the energy (E_5) of the emitted gluon is soft, i.e. $E_5 \le \delta_s\sqrt{s}/2$, or hard, i.e. $E_5 > \delta_s\sqrt{s}/2$. Correspondingly, the partonic real cross section can be written as

$$\hat{\sigma}^R = \hat{\sigma}^S + \hat{\sigma}^H, \quad (26)$$

where $\hat{\sigma}^S$ and $\hat{\sigma}^H$ are the contributions from the soft and the hard regions, respectively. $\hat{\sigma}^S$ contains all the soft divergences, which can be explicitly obtained after analytically integrating over the phase space of the emitted soft gluon. Second, in order to isolate the remaining collinear divergences from $\hat{\sigma}^H$, we should introduce another arbitrary small cutoff, called collinear cutoff δ_c, to further split the hard gluon phase space into two regions, according to whether the Mandelstam variables satisfy the collinear condition $-\delta_c s < u_{1,2} \equiv (p_{1,2} - p_5)^2 < 0$ or not. Thus, we have

$$\hat{\sigma}^H = \hat{\sigma}^{\mathrm{HC}} + \hat{\sigma}^{\overline{\mathrm{HC}}}, \quad (27)$$

where the hard collinear part $\hat{\sigma}^{\mathrm{HC}}$ contains the collinear divergences, which can be explicitly obtained after analytically integrating over the phase space of the emitted collinear gluon. The hard noncollinear part $\hat{\sigma}^{\overline{\mathrm{HC}}}$ is finite and can be numerically computed using standard Monte-Carlo integration techniques [30] and can be written in the form:

$$d\hat{\sigma}^{\overline{\mathrm{HC}}} = \frac{1}{2s}\overline{\sum}|M^{b\bar{b}}|^2 d\overline{\Gamma}_3. \quad (28)$$

Here $d\overline{\Gamma}_3$ is the hard noncollinear region of the three-body phase space.

In the next two subsections, we will discuss in detail the soft and the hard collinear gluon emission.

1. Soft gluon emission

In the soft limit, i.e. when the energy of the emitted gluon is small, with $E_5 \le \delta_s\sqrt{s}/2$, the matrix element squared $\overline{\sum}|M^R|^2$ for the process $b(p_1)\bar{b}(p_2) \to Z^0(p_3)A^0(p_4)g(p_5)$ can be simply factorized into the Born matrix element squared times an eikonal factor Φ_{eik}:

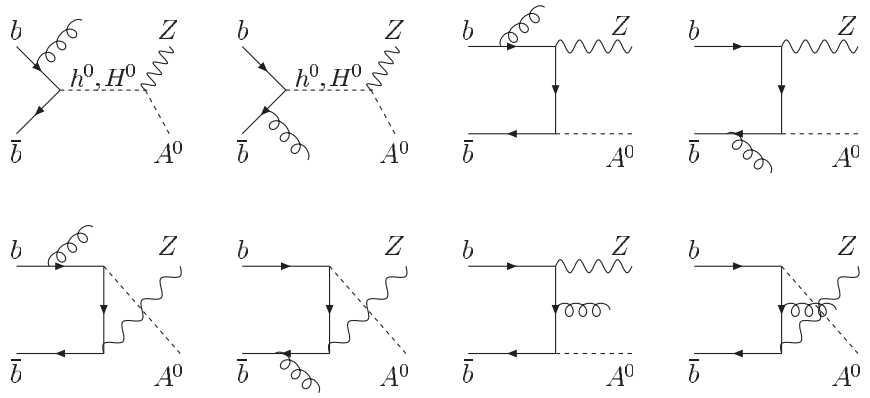

FIG. 4. Feynman diagrams for the real gluon emission contributions.

$$\overline{\sum}|M^R(b\bar{b} \to A^0Z^0 + g)|^2 \xrightarrow{\text{soft}} (4\pi\alpha_s\mu_r^{2\epsilon})\overline{\sum}|M^B|^2\Phi_{\text{eik}}, \tag{29}$$

where the eikonal factor Φ_{eik} is given by

$$\Phi_{\text{eik}} = C_F \frac{s}{(p_1 \cdot p_5)(p_2 \cdot p_5)}. \tag{30}$$

Moreover, the phase space in the soft limit can also be factorized as

$$d\Gamma_3(b\bar{b} \to A^0Z^0 + g) \xrightarrow{\text{soft}} d\Gamma_2(b\bar{b} \to A^0Z^0)dS, \tag{31}$$

where dS is the integration over the phase space of the soft gluon, which is given by [29]

$$dS = \frac{1}{2(2\pi)^{3-2\epsilon}} \int_0^{\delta_s\sqrt{s}/2} dE_5 E_5^{1-2\epsilon} d\Omega_{2-2\epsilon}. \tag{32}$$

Hence, the parton level cross section in the soft region can be expressed as

$$\hat{\sigma}^S = (4\pi\alpha_s\mu_r^{2\epsilon}) \int d\Gamma_2 \overline{\sum}|M^B|^2 \int dS\Phi_{\text{eik}}. \tag{33}$$

Using the approach of Ref. [29], after analytically integrating over the soft gluon phase space, Eq. (33) becomes

$$\hat{\sigma}^S = \hat{\sigma}^B \left[\frac{\alpha_s}{2\pi} \frac{\Gamma(1-\epsilon)}{\Gamma(1-2\epsilon)} \left(\frac{4\pi\mu_r^2}{s}\right)^{\epsilon}\right] \left(\frac{A_2^s}{\epsilon^2} + \frac{A_1^s}{\epsilon} + A_0^s\right), \tag{34}$$

with

$$A_2^s = 2C_F, \qquad A_1^s = -4C_F \ln\delta_s, \qquad A_0^s = 4C_F \ln^2\delta_s. \tag{35}$$

2. Hard collinear gluon emission

In the hard collinear region, i.e. $E_5 > \delta_s\sqrt{s}/2$ and $-\delta_c s < u_{1,2} < 0$, the emitted hard gluon is collinear to one of the incoming partons. As a consequence of the factorization theorems [31], the squared matrix element for $b\bar{b} \to A^0Z^0 + g$ can be factorized into the product of the Born squared matrix element and the Altarelli-Parisi splitting function for $b(\bar{b}) \to b(\bar{b})g$ [32,33], i.e.

$$\overline{\sum}|M^R(b\bar{b} \to A^0Z^0 + g)|^2 \xrightarrow{\text{collinear}} (4\pi\alpha_s\mu_r^{2\epsilon})\overline{\sum}|M^B|^2 \times \left(\frac{-2P_{bb}(z,\epsilon)}{zu_1} + \frac{-2P_{\bar{b}\bar{b}}(z,\epsilon)}{zu_2}\right), \tag{36}$$

where z denotes the fraction of incoming parton $b(\bar{b})$'s momentum carried by parton $b(\bar{b})$ with the emitted gluon taking a fraction $(1-z)$, and $P_{ij}(z,\epsilon)$ are the unregulated splitting functions in $n = 4 - 2\epsilon$ dimensions for $0 < z < 1$, which can be related to the usual Altarelli-Parisi splitting kernels [32] as $P_{ij}(z,\epsilon) = P_{ij}(z) + \epsilon P'_{ij}(z)$. Explicitly,

$$P_{bb}(z) = P_{\bar{b}\bar{b}}(z) = C_F \frac{1+z^2}{1-z} + C_F \frac{3}{2}\delta(1-z), \tag{37}$$

$$P'_{bb}(z) = P'_{\bar{b}\bar{b}}(z) = -C_F(1-z) + C_F \frac{1}{2}\delta(1-z). \tag{38}$$

Moreover, the three-body phase space can also be factorized in the collinear limit, and, for example, in the limit $-\delta_c s < u_1 < 0$ it has the following form [29]:

$$d\Gamma_3(b\bar{b} \to A^0Z^0 + g) \xrightarrow{\text{collinear}} d\Gamma_2(b\bar{b} \to A^0Z^0; s' = zs) \times \frac{(4\pi)^{\epsilon}}{16\pi^2\Gamma(1-\epsilon)} dz du_1 \times [(z-1)u_1]^{-\epsilon}. \tag{39}$$

Here the two-body phase space should be evaluated at the squared parton-parton energy zs. Thus, the three-body cross section in the hard collinear region is given by [29]

$$d\sigma^{\rm HC} = \hat{\sigma}^B\left[\frac{\alpha_s}{2\pi}\frac{\Gamma(1-\epsilon)}{\Gamma(1-2\epsilon)}\left(\frac{4\pi\mu_r^2}{s}\right)^{\epsilon}\right] \times\left(-\frac{1}{\epsilon}\right)\delta_c^{-\epsilon}[P_{bb}(z,\epsilon)G_{b/p}(x_1/z)G_{\bar{b}/p}(x_2) + P_{\bar{b}\bar{b}}(z,\epsilon)G_{\bar{b}/p}(x_1/z)G_{b/p}(x_2) + (x_1\leftrightarrow x_2)]\frac{dz}{z}\left(\frac{1-z}{z}\right)^{-\epsilon}dx_1dx_2, \quad (40)$$

where $G_{b(\bar{b})/p}(x)$ is the bare PDF.

C. Massless (anti)quark emission

In addition to the real gluon emission, a second set of real emission corrections to the inclusive production rate of $pp \to A^0Z^0$ at the NLO involves the processes with an additional massless (anti)quark in the final states:

$$gb \to bA^0Z^0, \qquad g\bar{b} \to \bar{b}A^0Z^0.$$

The relevant Feynman diagrams for massless (anti)quark emission (the diagrams for the antiquark emission are similar and are omitted here) are shown in Fig. 5.

Since the contributions from the real massless (anti)-quark emission contain the initial state collinear singularities, we also need to use the two-cutoff phase space slicing method [29] to isolate those collinear divergences. Because there is no soft divergence in the splitting of $g \to b\bar{b}$, we need only to separate the phase space into two regions: the collinear region and the hard noncollinear region. Thus, according to the approach shown in Ref. [29], the cross sections for the processes with an additional massless (anti)quark in the final states can be expressed as

$$d\sigma^{\rm add} = \sum_{(\alpha=g,\beta=b,\bar{b})}\hat{\sigma}^{\overline{C}}(\alpha\beta\to A^0Z^0+X)[G_{\alpha/p}(x_1)G_{\beta/p}(x_2)+(x_1\leftrightarrow x_2)]dx_1dx_2 + \hat{\sigma}^B\left[\frac{\alpha_s}{2\pi}\frac{\Gamma(1-\epsilon)}{\Gamma(1-2\epsilon)}\left(\frac{4\pi\mu_r^2}{s}\right)^{\epsilon}\right]\left(-\frac{1}{\epsilon}\right)\delta_c^{-\epsilon}[P_{bg}(z,\epsilon)G_{g/p}(x_1/z)G_{\bar{b}/p}(x_2)+G_{b/p}(x_1)P_{\bar{b}g}(z,\epsilon)G_{g/p}(x_2/z) + (x_1\leftrightarrow x_2)]\frac{dz}{z}\left(\frac{1-z}{z}\right)^{-\epsilon}dx_1dx_2, \quad (41)$$

where

$$P_{bg}(z) = P_{\bar{b}g}(z) = \tfrac{1}{2}[z^2+(1-z)^2], \qquad P'_{bg}(z) = P'_{\bar{b}g}(z) = -z(1-z). \quad (42)$$

The first term in Eq. (41) represents the noncollinear cross sections for the two processes, which can be written in the form:

$$d\hat{\sigma}^{\overline{C}} = \frac{1}{2s}\overline{\sum}|M^{\alpha\beta}|^2d\overline{\Gamma}_3, \quad (43)$$

where α and β denote the incoming partons in the partonic processes, and $d\overline{\Gamma}_3$ is the three-body phase space in the noncollinear region. The second term in Eq. (41) represents the collinear singular cross sections.

D. Mass factorization

As mentioned above, after adding the renormalized virtual corrections and the real corrections, the partonic cross sections still contain the collinear divergences, which can be absorbed into the redefinition of the PDF at NLO, in general called mass factorization [28]. This procedure in practice means that first we convolute the partonic cross section with the bare PDF $G_{\alpha/p}(x)$ and then rewrite $G_{\alpha/p}(x)$ in terms of the renormalized PDF $G_{\alpha/p}(x,\mu_f)$ in the numerical calculations. In the $\overline{\rm MS}$ scheme, the scale

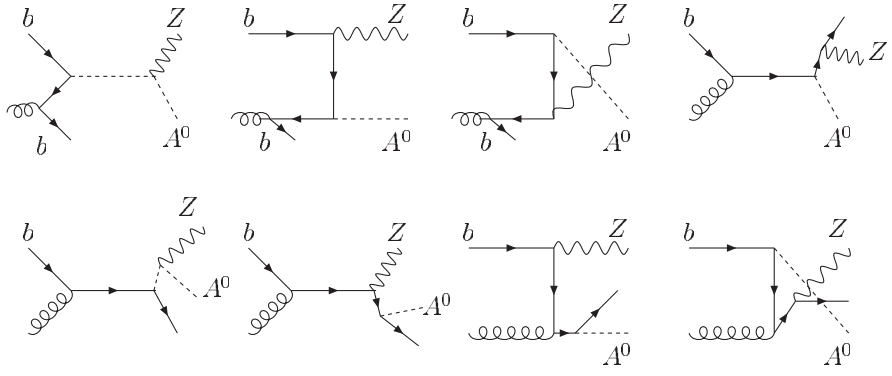

FIG. 5. Feynman diagrams for the emission of a massless bottom quark contribution.

dependent PDF $G_{\alpha/p}(x, \mu_f)$ is given by [29]

$$G_{\alpha/p}(x,\mu_f) = G_{\alpha/p}(x) + \sum_\beta \left(-\frac{1}{\epsilon}\right)\left[\frac{\alpha_s}{2\pi}\frac{\Gamma(1-\epsilon)}{\Gamma(1-2\epsilon)} \times \left(\frac{4\pi\mu_r^2}{\mu_f^2}\right)^\epsilon\right]\int_x^1 \frac{dz}{z} P_{\alpha\beta}(z) G_{\beta/p}(x/z). \quad (44)$$

After replacing the bare PDF by the renormalized $\overline{\rm MS}$ PDF and integrating out the collinear region of the phase space defined in the two-cutoff phase space slicing method [29], the resulting sum of Eq. (40) and the collinear part (the second term) of Eq. (41) yield the remaining $\mathcal{O}$ collinear contribution as [29]:

$$\sigma^{\rm coll} = \int \hat{\sigma}^B \left[\frac{\alpha_s}{2\pi}\frac{\Gamma(1-\epsilon)}{\Gamma(1-2\epsilon)}\left(\frac{4\pi\mu_r^2}{s}\right)^\epsilon\right]\Big\{\tilde{G}_{b/p}(x_1,\mu_f) G_{\bar{b}/p}(x_2,\mu_f) + G_{b/p}(x_1,\mu_f)\tilde{G}_{\bar{b}/p}(x_2,\mu_f) + \sum_{\alpha=b,\bar{b}}\left[\frac{A_1^{sc}(\alpha\to\alpha g)}{\epsilon} + A_0^{sc}(\alpha\to\alpha g)\right] G_{b/p}(x_1,\mu_f) G_{\bar{b}/p}(x_2,\mu_f) + (x_1 \leftrightarrow x_2)\Big\} dx_1 dx_2, \quad (45)$$

where

$$A_1^{sc}(b\to bg) = A_1^{sc}(\bar{b}\to\bar{b}g) = C_F(2\ln\delta_s + 3/2), \quad (46)$$

$$A_0^{sc} = A_1^{sc}\ln\left(\frac{s}{\mu_f^2}\right), \quad (47)$$

$$\tilde{G}_{\alpha(=b,\bar{b})/p}(x,\mu_f) = \sum_{\beta=g,\alpha}\int_x^{1-\delta_s\delta_{\alpha\beta}}\frac{dy}{y} \times G_{\beta/p}(x/y,\mu_f)\tilde{P}_{\alpha\beta}(y), \quad (48)$$

with

$$\tilde{P}_{\alpha\beta}(y) = P_{\alpha\beta}(y)\ln\left(\delta_c\frac{1-y}{y}\frac{s}{\mu_f^2}\right) - P'_{\alpha\beta}(y). \quad (49)$$

The NLO total cross section for $pp \to A^0 Z^0$ in the $\overline{\rm MS}$ factorization scheme is obtained by summing up the Born, virtual, soft, collinear, and hard noncollinear contributions. In terms of the above notations, we have

$$\sigma^{\rm NLO} = \int dx_1 dx_2 \{[G_{b/p}(x_1,\mu_f)G_{\bar{b}/p}(x_2,\mu_f) + (x_1\leftrightarrow x_2)](\hat{\sigma}^B + \hat{\sigma}^V + \hat{\sigma}^S + \hat{\sigma}^{\overline{\rm HC}})\} + \sigma^{\rm coll} + \sum_{(\alpha=g,\beta=b,\bar{b})}\int dx_1 dx_2 [G_{\alpha/p}(x_1,\mu_f)G_{\beta/p}(x_2,\mu_f) + (x_1\leftrightarrow x_2)]\hat{\sigma}^{\overline{C}}(\alpha\beta\to A^0Z^0 + X). \quad (50)$$

We note that the above expression contains no singularities, for $2A_2^V + A_2^s = 0$ and $2A_1^V + A_1^s + A_1^{sc}(b\to bg) + A_1^{sc}(\bar{b}\to\bar{b}g) = 0$. Namely, all the $1/\epsilon^2$ and $1/\epsilon$ terms cancel in $\sigma^{\rm NLO}$. The apparent logarithmic δ_s and δ_c dependent terms also cancel with the hard noncollinear cross section $\hat{\sigma}^{\overline{\rm HC}}$ after numerically integrating over its relevant phase space volume.

E. Real emission corrections and NLO total cross sections in the DRED scheme

In the end of Sec. III A, cf. Eqs. (21)–(25), we discussed the results of virtual corrections in the DRED scheme. Here we examine the real emission corrections and the NLO total cross section in the DRED scheme and compare them with those obtained in the DREG scheme. We find that the contributions from soft gluon emission remain the same, while the ones from hard collinear gluon emission and massless (anti)quark emission are different due to the difference in the parton splitting functions and the perturbative PDFs.

First, the splitting functions in the DRED scheme contain no ϵ parts, so that

$$P_{ij}(z,\epsilon)_{\rm DRED} = P_{ij}(z). \quad (51)$$

Thus, from Eqs. (45) and (51), we find the difference

$$\sigma^{\rm coll}{}_{\rm DREG} - \sigma^{\rm coll}{}_{\rm DRED} = -\frac{\alpha_s}{2\pi}\int\hat{\sigma}^B\Big\{\sum_\beta\int_{x_1}^{1-\delta_s\delta_{b\beta}}\frac{dy}{y}G_{\beta/p}(x_1/y,\mu_f)P'_{b\beta}(y)G_{\bar{b}/p}(x_2,\mu_f) + \sum_\beta\int_{x_2}^{1-\delta_s\delta_{\bar{b}\beta}}\frac{dy}{y}G_{\beta/p}(x_2/y,\mu_f)P'_{\bar{b}\beta}(y)G_{b/p}(x_1,\mu_f) + (x_1\leftrightarrow x_2)\Big\}dx_1dx_2. \quad (52)$$

Second, the perturbative PDFs defined in the DRED and the DREG schemes are different, and [34]

$$G_{\alpha/p}(x,\mu_f)_{\rm DREG} - G_{\alpha/p}(x,\mu_f)_{\rm DRED} = \frac{\alpha_s}{2\pi}\sum_\beta\int_x^1\frac{dy}{y}P'_{\alpha\beta}(x/y)G_{\alpha/p}(x,\mu_f)_{\rm DREG}. \quad (53)$$

After substituting them into the formula for calculating the Born level cross sections, cf. Eq. (4), we find the difference arising from the perturbative PDFs, at the $\mathcal{O}(\alpha_s)$ level, as:

$$\sigma^B{}_{\rm DREG} - \sigma^B{}_{\rm DRED} = \frac{\alpha_s}{2\pi}\int \hat{\sigma}^B\Big\{\sum_\beta \int_{x_1}^1 \frac{dy}{y} G_{\beta/p}(x_1/y,\mu_f)_{\rm DRED} P'_{b\beta}(y) G_{\bar{b}/p}(x_2,\mu_f)_{\rm DRED} + \sum_\beta \int_{x_2}^1 \frac{dy}{y} G_{\beta/p}(x_2/y,\mu_f)_{\rm DRED} P'_{\bar{b}\beta}(y) G_{b/p}(x_1,\mu_f)_{\rm DRED} + (x_1 \leftrightarrow x_2)\Big\} dx_1 dx_2. \quad (54)$$

Except the upper limit of the integral over y, the two expressions in Eqs. (52) and (54) are the same. After substituting Eqs. (25), (52), and (54) into Eq. (50), we find the relation between the two NLO total cross sections, separately calculated in the DREG and the DRED schemes, as follows:

$$\sigma^{\rm NLO}{}_{\rm DREG} - \sigma^{\rm NLO}{}_{\rm DRED} = \frac{\alpha_s}{2\pi}\int \hat{\sigma}^B\Big\{\sum_\beta \int_{1-\delta_s\delta_{b\beta}}^1 \frac{dy}{y} G_{\beta/p}(x_1/y,\mu_f) P'_{b\beta}(y) G_{\bar{b}/p}(x_2,\mu_f) + \sum_\beta \int_{1-\delta_s\delta_{\bar{b}\beta}}^1 \frac{dy}{y} \times G_{\beta/p}(x_2/y,\mu_f) P'_{\bar{b}\beta}(y) G_{b/p}(x_1,\mu_f) + (x_1 \leftrightarrow x_2)\Big\} dx_1 dx_2 - \frac{\alpha_s}{2\pi} C_F \sigma^B_{\rm DRED} + \mathcal{O}(\alpha_s^2). \quad (55)$$

Using the explicit expressions of the ϵ parts of the splitting functions P', cf. Eqs. (38) and (42), we find

$$\sigma^{\rm NLO}_{\rm DREG} = \sigma^{\rm NLO}_{\rm DRED} + \mathcal{O}(\alpha_s^2). \quad (56)$$

As expected, both schemes yield the same NLO total cross sections, up to $\mathcal{O}(\alpha_s^2)$.

F. Differential cross sections in transverse momentum and invariant mass

In this subsection, we present the differential cross section in the transverse momentum of Z^0 and A^0 bosons, respectively, and the invariant mass of the A^0Z^0 pair. Using the notations defined in Ref. [35], the differential distribution of the transverse momentum (p_T) and rapidity (y) of Z^0 boson for the processes

$$p(p_1) + p(p_2) \to Z^0(p_3) + A^0(p_4)[+g(p_5)/b(p_5)/\bar{b}(p_5)] \quad (57)$$

is given by

$$\frac{d^2\sigma}{dp_T dy} = 2p_T S \sum_{\alpha,\beta}\int_{x_1^-}^1 dx_1 \int_{x_2^-}^1 dx_2 x_1 G_{\alpha/p}(x_1,\mu_f) x_2 \times G_{\beta/p}(x_2,\mu_f)\frac{d^2\hat{\sigma}_{\alpha\beta}}{dt' du'}, \quad (58)$$

where $\sqrt{S}$ is the total center-of-mass energy of the collider, and

$$p_T^2 = \frac{T_2 U_2}{S} - m_{Z^0}^2, \qquad y = \frac{1}{2}\ln\Big(\frac{T_2}{U_2}\Big),$$
$$x_1^- = \frac{-T_2 - m_{Z^0}^2 + m_{A^0}^2}{S + U_2}, \quad (59)$$
$$x_2^- = \frac{-x_1 U_2 - m_{Z^0}^2 + m_{A^0}^2}{x_1 S + T_2},$$

with $T_2 = (p_2 - p_3)^2 - m_{Z^0}^2$ and $U_2 = (p_1 - p_3)^2 - m_{Z^0}^2$. The limits of integral over y and p_T are

$$-y^{\rm max}(p_T) \le y \le y^{\rm max}(p_T), \qquad 0 \le p_T \le p_T^{\rm max}, \quad (60)$$

with

$$y^{\rm max}(p_T) = \operatorname{arccosh}\Big(\frac{S + m_{Z^0}^2 - m_{A^0}^2}{2\sqrt{S(p_T^2 + m_{Z^0}^2)}}\Big),$$
$$p_T^{\rm max} = \frac{1}{2\sqrt{S}}\sqrt{(S + m_{Z^0}^2 - m_{A^0}^2)^2 - 4m_{Z^0}^2 S}. \quad (61)$$

The differential distribution with respect to p_T and y of A^0 is similar to the one of Z^0. The differential distribution with respect to the invariant mass M_{AZ} is given by

$$\frac{d\sigma}{dM_{AZ}} = \frac{2M_{AZ}}{S}\sum_{\alpha,\beta}\frac{d\mathcal{L}^{\alpha\beta}_{\mathcal{A}Z}}{d\tau}\hat{\sigma}_{\alpha\beta}(\tau S), \quad (62)$$

where $d\mathcal{L}^{\alpha\beta}_{\mathcal{A}Z}/d\tau$ is the parton luminosity, defined as:

$$\frac{d\mathcal{L}^{\alpha\beta}_{\mathcal{A}Z}}{d\tau} = \int_\tau^1 \frac{dx}{x}[G_{\alpha/p}(x,\mu_f) G_{\beta/p}(\tau/x,\mu_f)], \quad (63)$$

with

$$M_{AZ} \equiv \sqrt{(E_3 + E_4)^2 - (\vec{p}_3 + \vec{p}_4)^2} \ge (m_{A^0} + m_{Z^0}), \quad (64)$$

$$\tau \equiv M_{AZ}^2/S. \quad (65)$$

IV. NUMERICAL RESULTS

In the numerical calculations, we used the following set of SM parameters [36]:

$$\alpha_{ew}(m_W) = 1/128, \qquad m_W = 80.419\ \text{GeV},$$
$$m_Z = 91.1882\ \text{GeV}, \qquad m_t = 178\ \text{GeV}, \quad (66)$$
$$\alpha_s(M_Z) = 0.118.$$

The running QCD coupling $\alpha_s(Q)$ is evaluated at the two-loop order [37], and the CTEQ6M PDFs [38] are used throughout this paper to calculate various cross sections, either at the LO or the NLO. As to the Yukawa coupling of the bottom quark, we shall first use the $\overline{\rm MS}$ bottom quark mass, $m_b(m_b) = 4.25$ GeV, to evaluate the event rate, then

compare it with the one calculated using the QCD improved running mass to reduce the higher order QCD radiative corrections and, therefore, improve the perturbative calculations. The QCD improved running mass $m_b(Q)$, evaluated by the NLO formula [39], is

$$m_b(Q) = U_6(Q, m_t)U_5(m_t, m_b)m_b(m_b), \tag{67}$$

where the evolution factor U_f is

$$U_f(Q_2, Q_1) = \left(\frac{\alpha_s(Q_2)}{\alpha_s(Q_1)}\right)^{d^{(f)}}\left[1 + \frac{\alpha_s(Q_1) - \alpha_s(Q_2)}{4\pi} J^{(f)}\right],$$
$$d^{(f)} = \frac{12}{33 - 2f}, \qquad J^{(f)} = -\frac{8982 - 504f + 40f^2}{3(33 - 2f)^2}, \tag{68}$$

and f is the number of the active light quarks. For comparison, we list the QCD improved running bottom quark mass in Table I for various energy scales Q.

For large $\tan\beta$, the SUSY threshold correction to the bottom quark Yukawa couplings could be large, and it can be resummed by making the following replacement in the tree-level couplings to improve the perturbation calculations [39]:

$$m_b(Q) \to \frac{m_b(Q)}{1 + \Delta m_b(Q = M_{\rm SUSY})}, \tag{69}$$

$$\begin{aligned}\Delta m_b = {} & \frac{2\alpha_s(Q = M_{\rm SUSY})}{3\pi} M_{\tilde g}\mu \tan\beta I(m_{\tilde b_1}, m_{\tilde b_2}, M_{\tilde g}) \\ & + \frac{h_t^2}{16\pi^2}\mu A_t \tan\beta I(m_{\tilde t_1}, m_{\tilde t_2}, \mu) \\ & - \frac{g^2}{16\pi^2}\mu M_2 \tan\beta \sum_{i=1}^{2}\Big[(R^{\tilde t}_{i1})^2 I(m_{\tilde t_i}, M_2, \mu) \\ & + \frac{1}{2}(R^{\tilde b}_{i1})^2 I(m_{\tilde b_i}, M_2, \mu)\Big],\end{aligned} \tag{70}$$

where

$$\begin{aligned}I(a, b, c) = {} & \frac{1}{(a^2 - b^2)(b^2 - c^2)(a^2 - c^2)} \\ & \times\left(a^2 b^2 \log\frac{a^2}{b^2} + b^2 c^2 \log\frac{b^2}{c^2} + c^2 a^2 \log\frac{c^2}{a^2}\right),\end{aligned} \tag{71}$$

$$h_t = \frac{g m_t}{\sqrt{2} m_W \sin\beta}, \tag{72}$$

TABLE I. The QCD improved running bottom quark mass, evaluated at $Q = 250$, 500, and 750 GeV. The $\overline{\rm MS}$ bottom quark mass is taken to be $m_b(m_b) = 4.25$ GeV.

Q (GeV)	250	500	750
$m_b(Q)$ (GeV)	2.68	2.55	2.49

and $R^{\tilde t}$ and $R^{\tilde b}$ are the rotation matrices for defining the mass eigenstates of $\tilde t$ and $\tilde b$, respectively. We set $M_{\rm SUSY}$ in Δm_b to $m_{\tilde g}$ in our numerical calculations. Needless to say that when using the running bottom quark Yukawa coupling to evaluate cross sections, we shall subtract the corresponding (SUSY-)QCD corrections at the order α_s from the renormalization constant δm_b to avoid double counting in perturbative expansion of the strong coupling constant.

The values of the MSSM parameters taken in our numerical calculations were constrained within the minimal supergravity scenario (mSUGRA) [40], in which there are only five free input parameters at the grand unification scale. They are $m_{1/2}$, m_0, A_0, $\tan\beta$, and the sign of μ, where $m_{1/2}$, m_0, A_0 are, respectively, the universal gaugino mass, scalar mass, and the trilinear soft breaking parameter in the superpotential. Given those parameters, all the MSSM parameters at the weak scale are determined in the mSUGRA scenario by using the program package SUSPECT 2.3 [41]. In particular, we used the running Higgs masses at the m_Z scale, defined in the modified dimensional reduction ($\overline{\rm DR}$) scheme, which have included the full one-loop corrections, as well as the two-loop corrections controlled by the strong gauge coupling and the Yukawa couplings of the third generation fermions [41,42]. In our numerical calculations, we used the two-loop renormalization group equations (RGEs) presented in that program for calculating all the gauge couplings, the (third generation) Yukawa couplings, and the gaugino masses, while using one-loop RGE for the other supersymmetric parameters. In the following, we shall present our numerical studies based on the five sets of SUSY input parameters listed in Table II, which are consistent with all the existing experiment data [36]. We will also vary $\tan\beta$, m_0, and A_0 to examine their effects to various cross sections. For completeness, we also show the relevant SUSY output parameters in Table III. The QCD plus SUSY-QCD and SUSY-EW (electroweak) improved bottom quark running mass are listed in Table IV, which should be compared with those given in Table I, in which only the QCD running effect is included. For comparison, the QCD plus SUSY-QCD improved bottom quark running mass are separately listed in Table V.

TABLE II. Five sets of SUSY input parameters studied in this paper, within the mSUGRA scenario.

Set number	m_0 (GeV)	$m_{1/2}$ (GeV)	A_0 (GeV)	$\tan\beta$	Sign (μ)
1	150	180	300	40	+
2	150	400	300	40	+
3	200	160	100	40	−
4	250	160	100	40	−
5	400	160	100	40	−

TABLE III. The SUSY output parameters used in our numerical calculations, corresponding to the five sets of SUSY input parameters listed in Table II.

	$m_{\tilde{b}_{1(2)}}$ (GeV)	$m_{\tilde{t}_{1(2)}}$ (GeV)	$m_{\tilde{g}}$ (GeV)	$m_{A^0(h^0,H^0)}$ (GeV)	$A_{t(b)}$ (GeV)	μ (GeV)	α	$\cos\theta_{\tilde{t}(\tilde{b})}$
1	374.6(429.1)	339.7(457.7)	457.0	223.8(107.5223.9)	−256.5(−275.8)	235.3	−0.032	0.97(0.74)
2	764.3(822.0)	673.6(833.8)	940.0	458.3(115.5458.3)	−607.5(−750.9)	498.1	−0.027	0.47(0.71)
3	314.3(395.1)	305.5(425.1)	416.8	133.7(106.7134.1)	−263.9(−303.9)	−224.6	−0.143	0.62(−0.69)
4	330.8(408.6)	317.0(434.3)	419.9	155.0(107.2155.3)	−262.7(−303.6)	−228.8	−0.086	0.60(0.71)
5	396.1(467.5)	363.9(476.1)	431.9	233.0(108.4233.2)	−261.0(−304.9)	−249.4	−0.043	0.54(0.79)

TABLE IV. The QCD plus SUSY-QCD and SUSY-EW improved bottom quark running mass for the five sets of SUSY inputs listed in Table II, evaluated at $Q = 250$, 500, and 750 GeV.

Set number	1	2	3	4	5
$m_b(Q = 250, M_{\rm SUSY} = m_{\tilde{g}})$ (GeV)	2.35	2.41	3.18	3.16	3.10
$m_b(Q = 500, M_{\rm SUSY} = m_{\tilde{g}})$ (GeV)	2.24	2.29	3.03	3.01	2.96
$m_b(Q = 750, M_{\rm SUSY} = m_{\tilde{g}})$ (GeV)	2.18	2.23	2.95	2.93	2.88

TABLE V. The QCD plus SUSY-QCD improved bottom quark running mass for the five sets of SUSY inputs listed in Table II, evaluated at $M_{\rm SUSY} = m_{\tilde{g}}$, and $Q = 250$, 500, and 750 GeV.

Set number	1	2	3	4	5
$m_b(Q = 250, M_{\rm SUSY} = m_{\tilde{g}})$ (GeV)	2.15	2.14	3.71	3.66	3.53
$m_b(Q = 500, M_{\rm SUSY} = m_{\tilde{g}})$ (GeV)	2.04	2.04	3.53	3.49	3.36
$m_b(Q = 750, M_{\rm SUSY} = m_{\tilde{g}})$ (GeV)	1.99	1.98	3.44	3.39	3.27

As for the renormalization and factorization scales, we always chose $\mu_r = m_{\rm av} \equiv (m_{A^0} + m_{Z^0})/2$ and $\mu_f = m_{\rm av}$, unless specified otherwise.

A. LO total cross section

In Figs. 6 and 7, we first compare the LO total cross sections of $pp \to A^0 Z^0$ via $b\bar{b}$ annihilation with the ones via gluon fusion and Drell-Yan processes, respectively. Here we use the $\overline{\rm MS}$ bottom quark mass $m_b(m_b) = 4.25$ GeV, without including the effect from QCD running. Our numerical results are different from the ones presented in Ref. [18], because the updated SUSY parameters are used instead of the earlier input parameters used in Ref. [18], which have already been ruled out by recent experiments. As shown in Figs. 6 and 7, the LO total cross sections via $b\bar{b}$ annihilation and Drell-Yan processes increase with $\tan\beta$, while the ones via gluon fusion process are relatively larger for low and high values of $\tan\beta$ but become smaller for intermediate values of $\tan\beta$. Moreover, all the LO rates decrease when m_{A^0} increases. Figures 6 and 7 also show that, in most of the chosen parameter range, $b\bar{b}$ contributions are much larger than the ones from gluon fusion and Drell-Yan processes, especially for large $\tan\beta$ and small m_{A^0}, where the total cross sections from the $b\bar{b}$ contributions can reach a few hundred femtobarn.

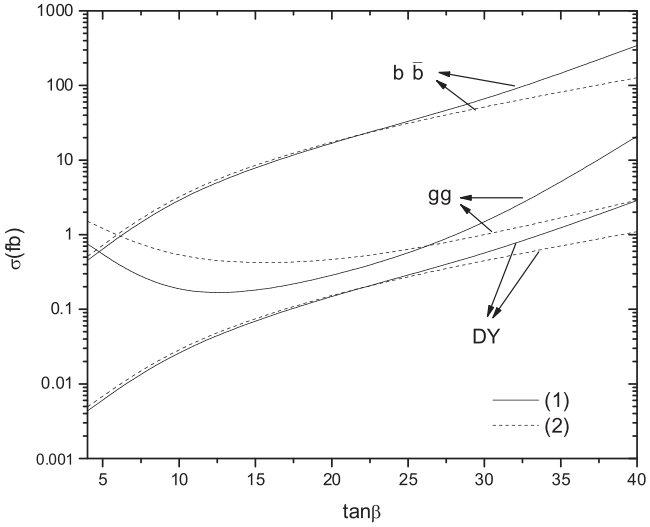

FIG. 6. LO total cross sections of $pp \to A^0 Z^0$ via $b\bar{b}$ annihilation, compared with the ones from gluon fusion and Drell-Yan processes at the LHC, as a function of $\tan\beta$ with $m_b(m_b) = 4.25$ GeV, assuming: (1) $m_0 = 200$ GeV, $m_{1/2} = 160$ GeV, $A_0 = 100$ GeV, and $\mu < 0$; (2) $m_0 = 150$ GeV, $m_{1/2} = 180$ GeV, $A_0 = 300$ GeV, and $\mu > 0$.

B. Cutoff dependence

In Fig. 8, we show the dependence of the NLO QCD predictions on the two arbitrary theoretical cutoff scales δ_s and δ_c, introduced in the two-cutoff phase space slicing method, where we have set $\delta_c = \delta_s/50$ to simplify the study and used QCD plus SUSY improved bottom quark Yukawa coupling. The NLO total cross section can be separated into two classes of contributions. One is the $2 \to 2$ rate contributed by the Born level, and the $\mathcal{O}(\alpha_s)$ virtual, soft, and hard collinear real emission corrections, denoted as $\hat{\sigma}^B$, $\hat{\sigma}^V$, $\hat{\sigma}^S$, and $\sigma^{\rm coll}$ in Eq. (50). Another is the $2 \to 3$ rate contributed by the $\mathcal{O}(\alpha_s)$ hard noncollinear real emission corrections, denoted as $\hat{\sigma}^{\overline{\rm HC}}$ and $\hat{\sigma}^{\overline{C}}$ in Eq. (50). As noted in the previous section, the $2 \to 2$ and $2 \to 3$ rates depend individually on δ_s and δ_c, but their sum should not depend on any of the theoretical cutoff scales. This is

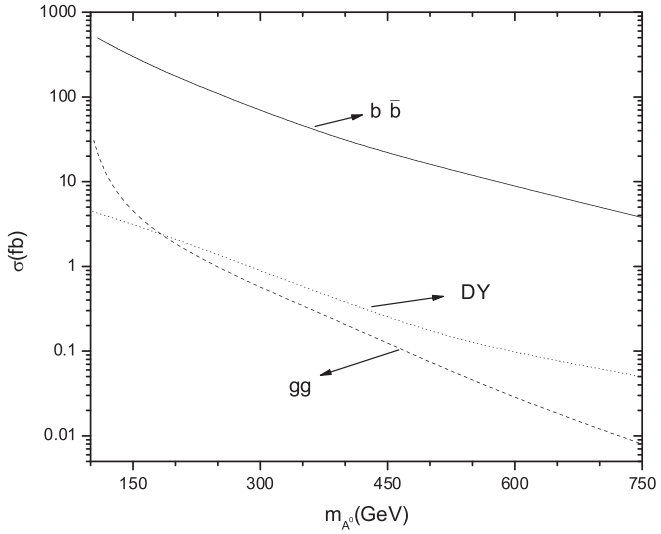

FIG. 7. LO total cross sections of $pp \to A^0Z^0$ via $b\bar{b}$ annihilation, compared with the ones from gluon fusion and Drell-Yan process at the LHC, as a function of m_{A^0} with $m_b(m_b) = 4.25$ GeV, assuming: $m_{1/2} = 160$ GeV, $A_0 = 100$ GeV, $\tan\beta = 40$, and $\mu < 0$.

clearly illustrated in Fig. 8 for two different sets of SUSY parameters. We find that $\sigma_{\rm NLO}$ is almost unchanged for δ_s between 5×10^{-5} and 10^{-2}, which is about 200 and 28 fb, respectively, for the two different sets of SUSY parameters. Therefore, we take $\delta_s = 10^{-4}$ and $\delta_c = \delta_s/50$ in the numerical calculations below.

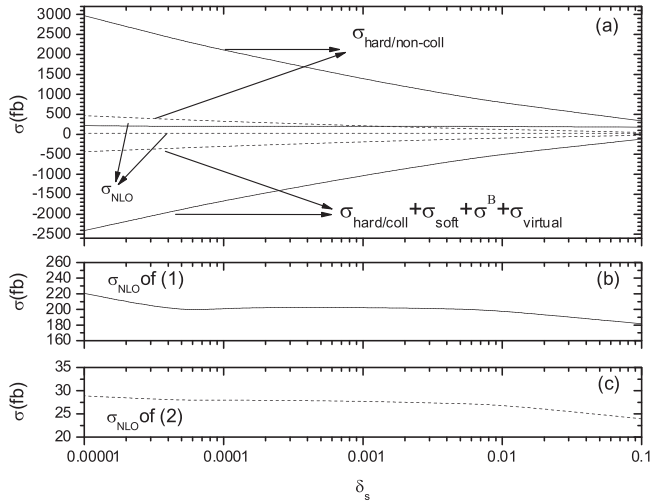

FIG. 8. Dependence of the NLO total cross sections for the A^0Z^0 production at the LHC on the theoretical cutoff scale δ_s with $\delta_c = \delta_s/50$, assuming: (1) $m_0 = 200$ GeV, $m_{1/2} = 160$ GeV, $A_0 = 100$ GeV, $\tan\beta = 40$, and $\mu < 0$; (2) $m_0 = 150$ GeV, $m_{1/2} = 180$ GeV, $A_0 = 300$ GeV, $\tan\beta = 40$, and $\mu > 0$. Here we take $m_b(m_b) = 4.25$ GeV. In (a), the solid and the dotted curves are the results for model (1) and (2), respectively.

C. m_{A^0} dependence

In Fig. 9, we show the total cross sections of $pp \to A^0Z^0$ at the LHC as a function of m_{A^0} for $\tan\beta = 10$ and 40, respectively, assuming $m_{1/2} = 160$ GeV, $A_0 = 100$ GeV, and $\mu < 0$. We considered the LO total cross sections in three different cases, i.e. using (I) $\overline{\rm MS}$ bottom quark mass at the scale m_b, (II) QCD improved bottom quark running mass at the scale m_{A^0}, and (III) QCD plus SUSY improved bottom quark running mass at the scale m_{A^0}, respectively. We also considered the NLO total cross sections for the cases of (II) and (III). Figure 9 shows that the LO and NLO total cross sections get smaller with the increasing m_{A^0}, and

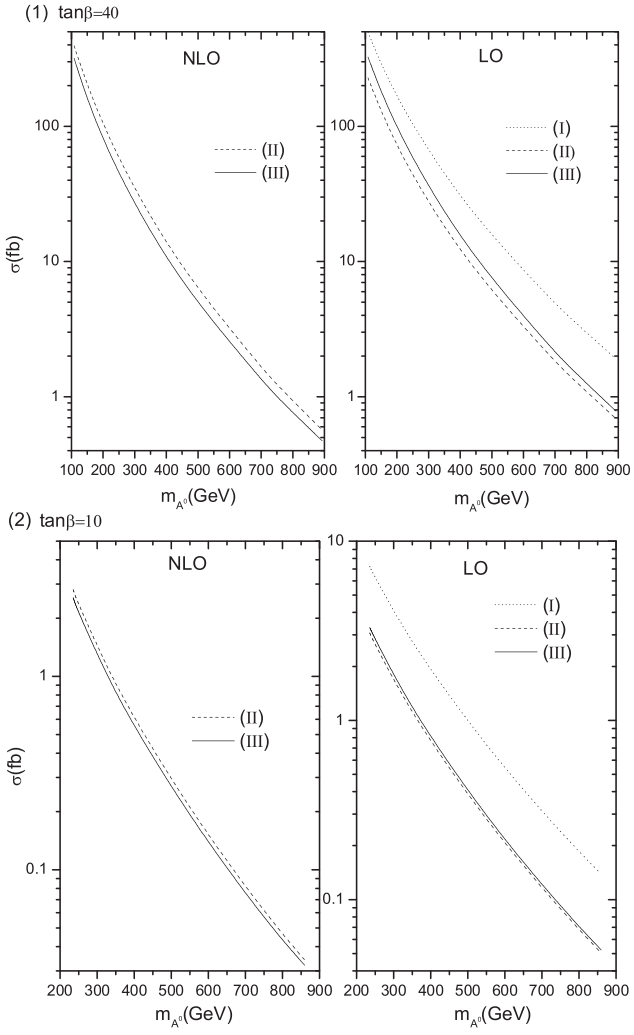

FIG. 9. Dependence of the total cross section of the A^0Z^0 production at the LHC on m_{A^0}, assuming $m_{1/2} = 160$ GeV, $A_0 = 100$ GeV, and $\mu < 0$ for $\tan\beta = 40$ in (1) and $\tan\beta = 10$ in (2). Three different calculations were done by using: (I) $\overline{\rm MS}$ bottom quark mass at the scale m_b, (II) QCD improved bottom quark running mass at the scale m_{A^0}, and (III) QCD plus SUSY improved bottom quark running mass at the scale m_{A^0}, respectively, to evaluate the bottom quark Yukawa coupling.

the results for $\tan\beta = 10$ in Fig. 9(2) are much smaller than the ones for $\tan\beta = 40$ in Fig. 9(1). For small m_{A^0} ($<$ 160 GeV) the LO total cross sections in Fig. 9(1) can be larger than 100 fb. The contributions from the QCD running m_b mass effects and the SUSY improved m_b corrections are significant; for example, in Fig. 9(1) when $m_{A^0} \simeq 155$ GeV and $\tan\beta = 40$, the LO total cross sections are about 270, 120, and 185 fb for the three cases, respectively. Moreover, Fig. 9 shows that the NLO QCD corrections can either enhance or suppress the total rate, and the $\mathcal{O}(\alpha_s)$ contribution is in general a few tens percent of the total rate, as described below. Define the K factor as the ratio of the NLO to LO total cross sections, calculated using the CTEQ6M PDFs. We show in Fig. 10 the dependence of the K factor on m_{A^0} for A^0Z^0 production, based on the results of case (II) in Fig. 9. Namely, the QCD improved bottom quark running mass is used for calculating the total cross section at the LO and the NLO. Figure 10 shows that, in general, the K factor becomes smaller with the increasing m_{A^0}. For example, curve (a) in Fig. 10(1) shows that when m_{A^0} varies from 108 to 900 GeV, the K factor varies from 1.72 to 0.82, and curve (a) in Fig. 10(2) shows that when m_{A^0} varies from 235 to 860 GeV, the K factor varies from 0.91 to 0.68. The contributions to the K factors, shown as curve (a), in both Figs. 10(1) and 10(2) come from the pure QCD corrections, shown as curve (b), and SUSY-QCD corrections, shown as curve (c). The former includes both the virtual and the real emission contributions originated from pure QCD corrections, while the latter consists of only virtual corrections. As expected, the K factor contributed by the pure QCD corrections is under control, of a few tens percent, when the QCD improved bottom quark running mass is used to evaluate the Yukawa coupling of the bottom quark. On the other hand, the SUSY-QCD corrections could become large as m_{A^0} decreases, especially for large $\tan\beta$. For example, in Fig. 10(1), for $\tan\beta = 40$, when $m_{A^0} \simeq 108$ GeV, the K factor of SUSY-QCD corrections is about 0.8, which dominates the overall K factor. Hence, to improve the convergence of the perturbation calculations in the case of large $\tan\beta$, we could use the SUSY improved bottom quark running mass to evaluate the Yukawa coupling of the bottom quark. More on SUSY-QCD corrections will be discussed below. We have also examined the contributions from the box diagrams shown in Fig. 3. The pure QCD box diagram contribution, arising from Figs. 3(a) and 3(c), is ultraviolet finite but not infrared finite. For $\tan\beta = 40$ the finite part of the pure QCD box diagram contribution becomes more important for large m_{A^0}, and its effect is to decrease the total rate. On the contrary, the SUSY-QCD box diagram contribution, arising from Figs. 3(b) and 3(d), is free of any singularity and is small numerically.

Figure 11 shows the dependence of the K factors on m_{A^0} for A^0Z^0 production, based on the results of case (III) in Fig. 9. Namely, the QCD plus SUSY improved bottom

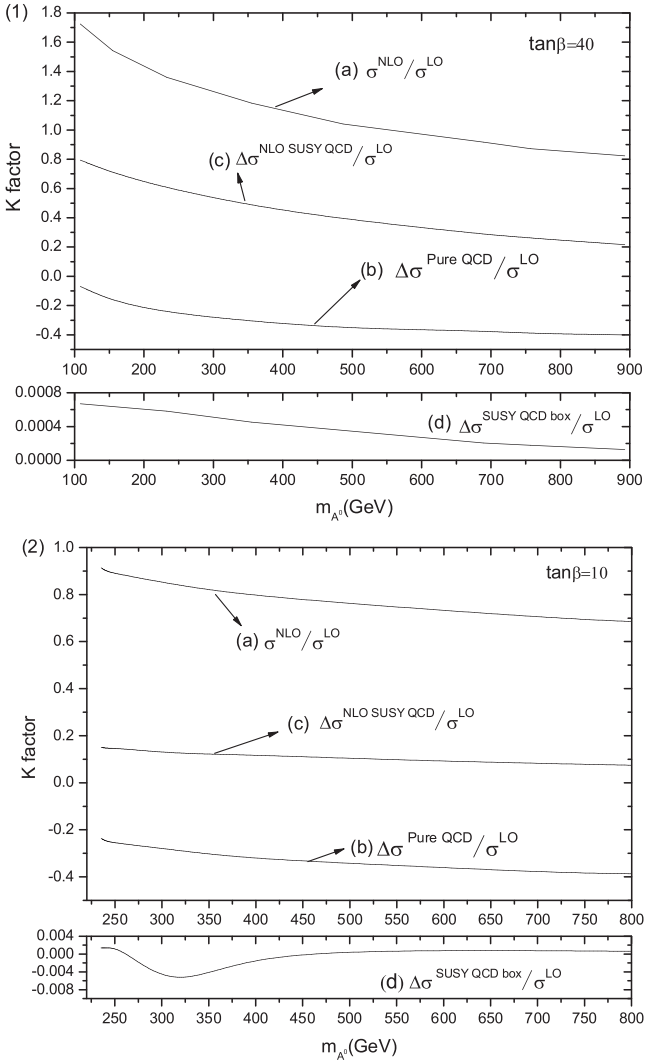

FIG. 10. K factor, defined as $\sigma_{\rm NLO}/\sigma_{\rm LO}$, for the A^0Z^0 production at the LHC as a function of m_{A^0}, using the QCD improved running m_b to evaluate the bottom quark Yukawa coupling, assuming $m_{1/2} = 160$ GeV, $A_0 = 100$ GeV, and $\mu < 0$ for $\tan\beta = 40$ in (1) and $\tan\beta = 10$ in (2). The full K factor is shown as curve (a), which includes the pure QCD corrections, shown as curve (b), and SUSY-QCD corrections, shown as curve (c). The contribution from the SUSY-QCD box diagrams is also separately shown as curve (d) for comparison.

quark running Yukawa coupling is used for calculating the total cross section at the LO and the NLO. Generally, the K factor decreases with m_{A^0}. For example, for $\tan\beta = 40$, when m_{A^0} varies from 108 to 900 GeV, the K factor corresponding to curve (a) ranges from 0.98 to 0.61, which contains two parts: the pure QCD corrections, shown as curve (b), and SUSY-QCD corrections, shown as curve (c). As compared to the results in Fig. 10(1), we find that the SUSY-QCD correction, shown as curve (c), has been largely suppressed. For instance, the K factor of SUSY-QCD corrections drops from 0.8, in Fig. 10(1), to 0.05, in Fig. 11, for $m_{A^0} \simeq 108$ GeV, while the other SUSY pa-

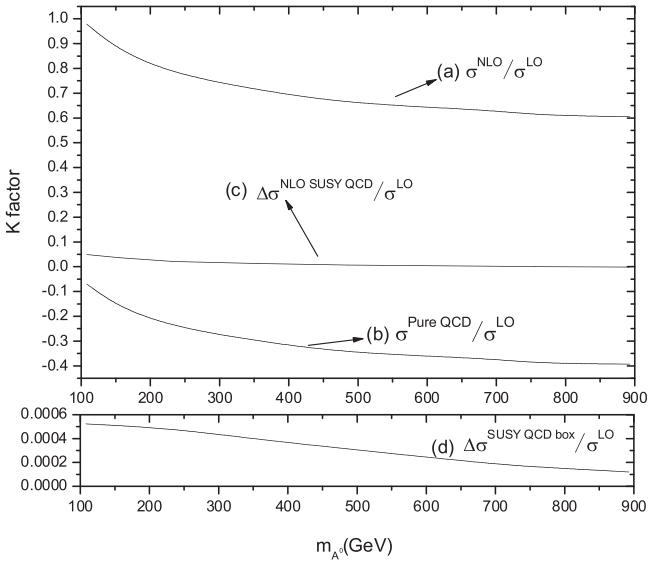

FIG. 11. K factor, defined as $\sigma_{\rm NLO}/\sigma_{\rm LO}$, for the A^0Z^0 production at the LHC as a function of m_{A^0}, using the QCD plus SUSY improved bottom quark Yukawa coupling, assuming $m_{1/2} = 160$ GeV, $A_0 = 100$ GeV, $\mu < 0$, and $\tan\beta = 40$. The full K factor is shown as curve (a), which includes the pure QCD corrections, shown as curve (b), and SUSY-QCD corrections, shown as curve (c). The contribution from the SUSY-QCD box diagrams is also separately shown as curve (d) for comparison.

rameters are identical in both calculations. This is because using the SUSY improved running m_b to evaluate the LO cross section, we have already included the dominant NLO SUSY-QCD corrections. Therefore, we shall use the QCD plus SUSY improved bottom quark running mass in the following numerical analysis for both the LO and the NLO calculations, unless specified otherwise.

D. SUSY-QCD corrections in heavy mass limit

It is instructive to examine the results of Figs. 10(1) and 11 in the heavy mass limit, where all the SUSY mass parameters except m_{A^0} are of the same size and tend to be heavy, i.e. $M_{\tilde{Q}} = M_{\tilde{D}} = \mu = A_b = M_{\tilde{g}} \equiv M_{\rm SUSY} \gg m_Z$. In the heavy mass limit, the SUSY-QCD box diagram contribution, arising from Figs. 3(b) and 3(d), is suppressed by powers of $M_{\rm SUSY}$ and can be neglected. This is confirmed by our numerical calculation which shows that the SUSY-QCD box contribution is generally below 0.1% of the total rate. Hence, we shall examine the effect of SUSY-QCD corrections in the heavy mass limit to the virtual diagrams shown in Figs. 2(a)–2(g) and compare the analytical result with our numerical calculations.

Since our aim is to examine the NLO SUSY-QCD effect in this part of study, we shall use the LO bottom quark Yukawa coupling (with $m_b = 4.25$ GeV) to evaluate the relevant tree-level vertices. Keeping only terms at $\mathcal{O}(\alpha_s)$ that are not suppressed by negative powers of heavy mass $M_{\rm SUSY}$ in the heavy mass limit, the one-loop SUSY-QCD correction to the individual diagram in Fig. 2 yields the following corrections. After stripping off the Born level matrix element (including all the vertex and propagator factors), the multiplicative factor of the s-channel diagram with the h^0 propagator, cf. Fig. 2(a), is given by

$$F_{(a)h^0} = -\frac{g_s^2}{12\pi^2}(1 + \cot\alpha), \tag{73}$$

where α is the mixing angle of the two CP-even Higgs bosons [2]. Note that Eq. (73) is in agreement with the one shown in Ref. [43]. Similarly, the multiplicative factor of the s-channel diagram with the H^0 propagator, cf. Fig. 2(a), is given by

$$F_{(a)H^0} = -\frac{g_s^2}{12\pi^2}(1 - \tan\alpha). \tag{74}$$

The multiplicative factor of the t- and u-channel diagrams, cf. Fig. 2(c) or Fig. 2(d), is given by

$$F_{(c)A^0} = F_{(d)A^0} = -\frac{g_s^2}{12\pi^2}(1 + \cot\beta). \tag{75}$$

The multiplicative factor for the sum of Figs. 2(b) and 2(g) is zero. This is because, after adding the wave function renormalization factor for the external bottom quark line, the renormalized $Zb\bar{b}$ vertex vanishes in the heavy mass limit. (Again, we have dropped any term that is suppressed by negative powers of the heavy mass scale $M_{\rm SUSY}$.) Similarly, the multiplicative factor for the sum of Figs. 2(e) and 2(f) is zero.

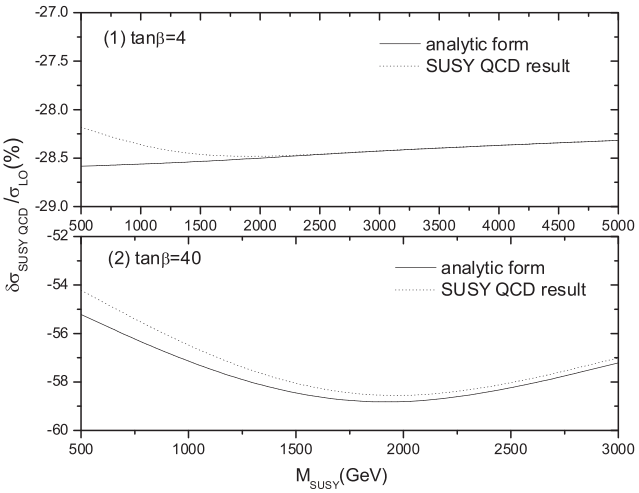

FIG. 12. Comparison of the SUSY-QCD corrections, denoted as $\delta\sigma_{\rm SUSY-QCD}/\sigma_{\rm LO}$, for the A^0Z^0 production at the LHC. The results of using the complete numerical calculation (dashed curves) and the approximate analytical forms (solid curves) in the heavy mass limit are separately shown as a function of $M_{\rm SUSY}$ with $\tan\beta = 4$ and 40, respectively, assuming $m_{A^0} = 150$ GeV and $M_{\tilde{Q}} = M_{\tilde{D}} = \mu = A_b = M_{\tilde{g}} \equiv M_{\rm SUSY}$. Here the LO cross section is calculated by using the $\overline{\rm MS}$ bottom quark mass.

Given the above multiplicative factors, we can calculate the SUSY-QCD correction to the total cross section for $pp \to A^0 Z^0$ production at the LHC and compare it with the complete numerical calculation described in Sec. III. The results in the heavy mass limit are shown in Fig. 12, which shows that the agreement becomes better for larger value of $M_{\rm SUSY}$. Hence, this provides a consistent check on our complete numerical calculations.

E. tanβ dependence

In Figs. 13(1) and 13(2), the total cross sections for $pp \to A^0 Z^0$ at the LHC are plotted as a function of tanβ for two representative values of $m_{1/2}$ and m_0, respectively. In Fig. 13(2), when tanβ ranges between 4 and 40, m_{A^0} varies from 330 to 223 GeV and from 660 to 458 GeV for $m_{1/2} = 180$ and 400 GeV, respectively. From Fig. 13(2) we can clearly see that the LO and the NLO total cross sections are enhanced with the increasing tanβ and decreased with the increasing $m_{1/2}$. For large tanβ (> 40) and $m_{1/2} =$ 180 GeV, the LO and the NLO total cross sections can be over 30 fb. The features in Fig. 13(1) are similar to the ones in Fig. 13(2), but, in general, the total cross sections are larger than later. For example, for large tanβ(>40) and $m_0 = 200$ GeV, both the LO and the NLO total cross sections can reach about hundreds of femtobarn.

Figure 14 shows the dependence of the K factors on tanβ, based on the results in Fig. 13, where the K factor increases with the increasing tanβ. For the results of Fig. 13(1), the K factor varies from 0.69 to 0.90 and from 0.65 to 0.92 for $m_0 = 200$ and 400 GeV, respectively. For the results of Fig. 13(2), the K factor varies from 0.70 to 0.74 and from 0.62 to 0.63 for $m_{1/2} = 180$ and 400 GeV, respectively.

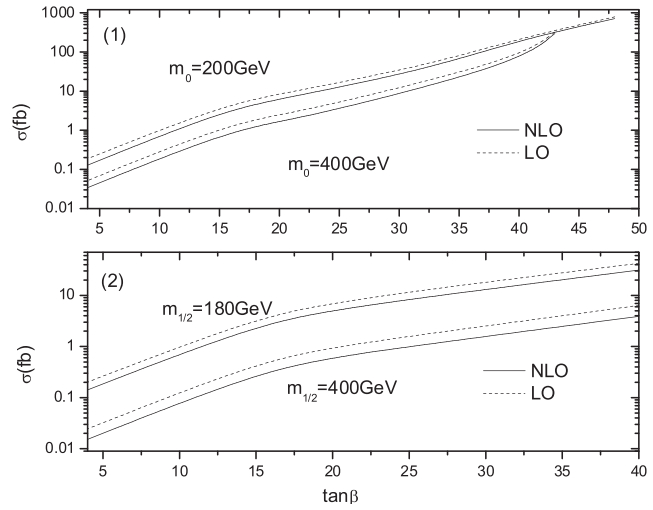

FIG. 13. Dependence of the total cross sections for the $A^0 Z^0$ production at the LHC on tanβ, assuming: (1) $m_0 = 200$ and 400 GeV, respectively, $m_{1/2} = 160$ GeV, $A_0 = 100$ GeV, and $\mu < 0$; (2) $m_0 = 150$ GeV, $m_{1/2} = 180$ and 400 GeV, respectively, $A_0 = 300$ GeV, and $\mu > 0$.

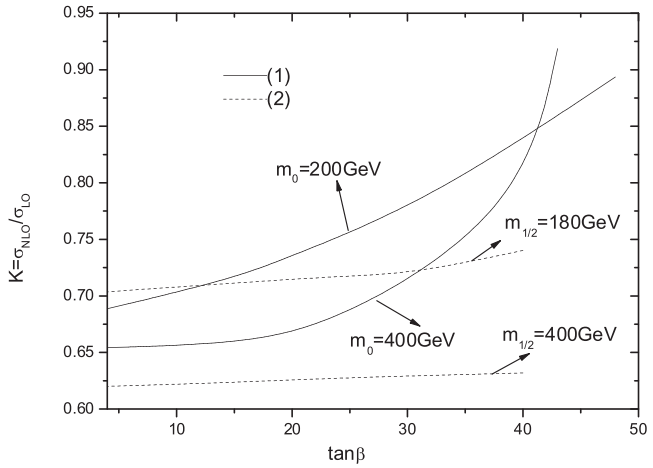

FIG. 14. Dependence of the K factor, defined as $\sigma_{\rm NLO}/\sigma_{\rm LO}$, on tan$\beta$ for the $A^0 Z^0$ production at the LHC, assuming: (1) $m_0 = 200$ and 400 GeV, respectively, $m_{1/2} = 160$ GeV, $A_0 = 100$ GeV, and $\mu < 0$; (2) $m_0 = 150$ GeV, $m_{1/2} = 180$ and 400 GeV, respectively, $A_0 = 300$ GeV, and $\mu > 0$.

F. μ_r/μ_f dependence

Figure 15 shows the dependence of the total cross sections for $pp \to A^0 Z^0$ production at the LHC on the renormalization scale (μ_r) and the factorization scale (μ_f), with $\mu_r = \mu_f$. The case (1) is for $\mu < 0$, and the case (2) is for

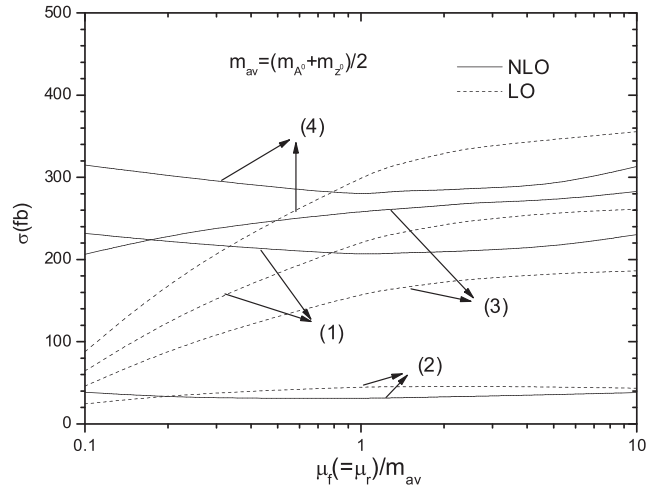

FIG. 15. Dependence of the total cross sections on the renormalization/factorization scale ($\mu_r = \mu_f$) for the $A^0 Z^0$ production at the LHC, assuming: (1) $m_0 = 200$ GeV, $m_{1/2} =$ 160 GeV, $A_0 = 100$ GeV, tan$\beta = 40$, and $\mu < 0$; (2) $m_0 = 150$ GeV, $m_{1/2} = 180$ GeV, $A_0 = 300$ GeV, tan$\beta =$ 40, and $\mu > 0$. Here the QCD plus SUSY improved bottom quark Yukawa coupling is used. The case of the curves (3) is similar to (1), but in (3) the pure QCD running bottom quark mass is used instead. The case of the curves (4) is similar to (1), but in (4) the contribution from the SUSY-EW correction in the running bottom quark Yukawa coupling is not included, namely, only the pure QCD and SUSY-QCD corrections are included.

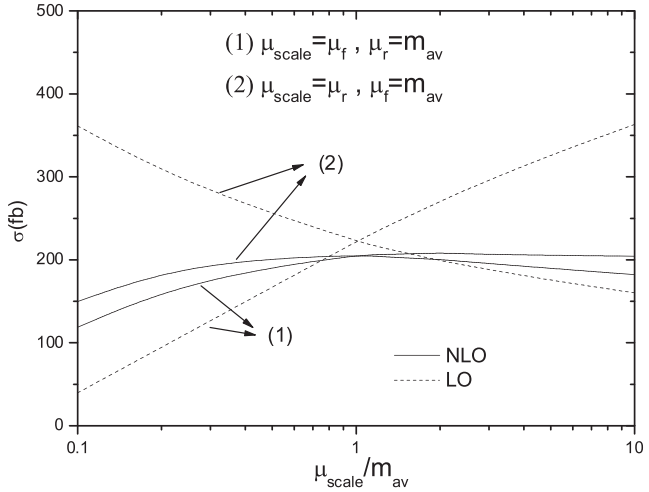

FIG. 16. Dependence of the total cross sections on the factorization scale (μ_f), labeled as case (1), or renormalization scale (μ_r), labeled as case (2), for the A^0Z^0 production at the LHC, assuming: $m_0 = 200$ GeV, $m_{1/2} = 160$ GeV, $A_0 = 100$ GeV, $\tan\beta = 40$, and $\mu < 0$. Here the QCD plus SUSY improved bottom quark Yukawa coupling is used and $m_{\rm av} = (m_{A^0} + m_{Z^0})/2$.

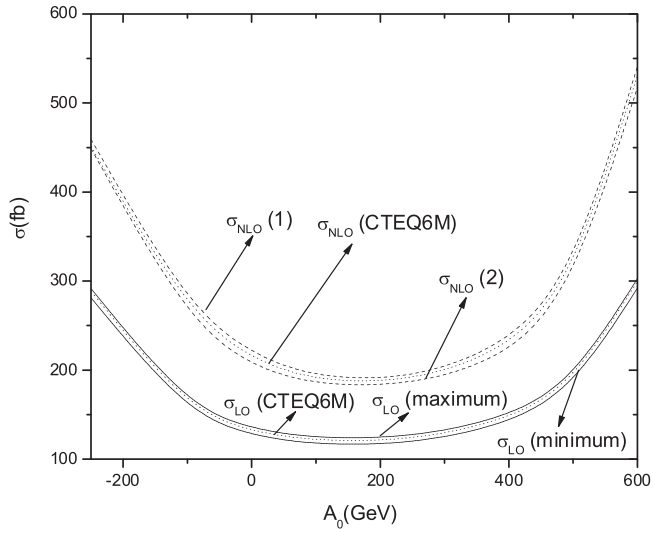

FIG. 17. The PDF dependence of the total cross sections for $pp \to A^0Z^0$ production at the LHC, as a function of A_0, assuming $m_0 = 250$ GeV, $m_{1/2} = 160$ GeV, $\tan\beta = 40$, and $\mu < 0$. Here the QCD running bottom quark mass is used to evaluate the bottom quark Yukawa coupling.

$\mu > 0$. In both cases, the scale dependence of the NLO total cross section is smaller than that of the LO cross section. For example, the LO cross sections vary from 65 to 261 fb and 25 to 45 fb when $\mu_r = \mu_f$ ranges between $0.1m_{\rm av}$ and $10m_{\rm av}$, while the NLO ones vary from 230 to 232 fb and 38 to 39 fb, in case (1) and case (2), respectively. Here the QCD plus SUSY improved bottom quark Yukawa coupling is used. For comparison, we also show the results of the other two calculations. The case (3) is similar to the case (1), but in (3) the pure QCD running bottom quark mass is used instead. The case (4) is similar to the case (1), but in (4) the contribution from the SUSY-EW correction in the running bottom quark Yukawa coupling is not included; namely, only the pure QCD and SUSY-QCD corrections are included.

To further investigate the scale dependence in case (1), with $\mu < 0$, we study the scale dependence of the total cross section on the renormalization scale (μ_r) and the factorization scale (μ_f) separately in Fig. 16. Here the QCD plus SUSY improved bottom quark Yukawa coupling is used. We find that in either case, whether we fixed μ_r and let μ_f vary or vice versa, the NLO rate is less dependent on the scale than the LO rate.

Hence, when applying the usual prescription to estimate the scale dependence, i.e. varying the scale around $m_{\rm av}$ by a factor of 2, the NLO cross sections vary by around 10% to 20%, cf. Figs. 15 and 16.

G. PDF uncertainty

To estimate the uncertainties in the total cross sections due to the uncertainty of PDFs, we take the 41 sets of CTEQ6.1 PDFs to calculate the LO and NLO rates [44]. As shown in Fig. 17, the LO result of using the CTEQ6M PDF lies between the maximum ($\sigma_{\rm max}$) and minimum ($\sigma_{\rm min}$) LO rates. The NLO total cross sections are then calculated using three different PDF sets, one of which is CTEQ6M; the other two are the ones that give the maximum and the minimum LO rates, respectively. The total cross sections for $pp \to A^0Z^0$ production at the LHC, as a

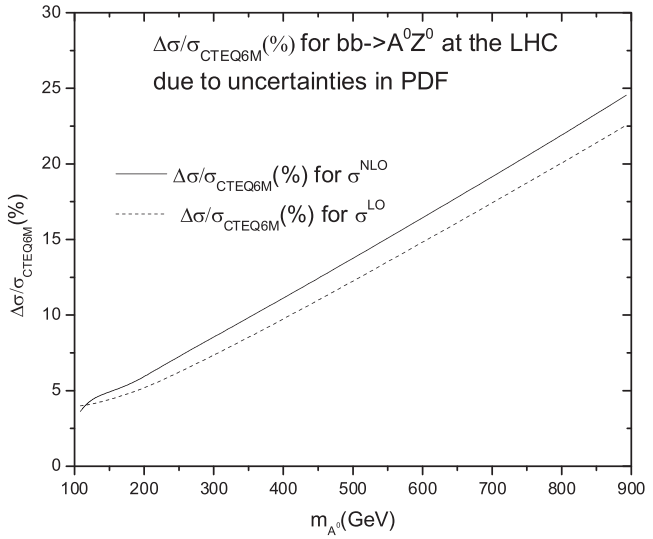

FIG. 18. The PDF dependence of the total cross sections for $pp \to A^0Z^0$ at the LHC as a function of m_{A^0}, assuming $A_0 = 100$ GeV, $m_{1/2} = 160$ GeV, $\tan\beta = 40$, and $\mu < 0$. Here the QCD running bottom quark mass is used to evaluate the bottom quark Yukawa coupling.

function of the trilinear coupling A_0, for the above mentioned PDFs are shown in Fig. 17, where we have used the QCD running mass to evaluate the bottom quark Yukawa coupling. It turns out that the PDF uncertainties [defined here as $\pm(\sigma_{\max} - \sigma_{\min})/(\sigma_{\max} + \sigma_{\min})$] in the LO and NLO total cross sections are about the same, when the QCD running m_b is used. For example, when $A_0 =$ 100 GeV, the PDF uncertainties are $\pm 2.9\%$ at the LO and $\pm 3.0\%$ at the NLO, respectively.

Figure 18 shows the PDF uncertainties [defined here as Eq. (3) in Ref. [45]] in the LO and NLO total cross sections for $pp \to A^0 Z^0$ production at the LHC, as a function of m_{A^0}. Here we also used the QCD running mass to evaluate the bottom quark Yukawa coupling. It turns out that the NLO rate has a slightly larger uncertainty than the LO rate due to the PDF uncertainties, especially at large m_{A^0}. Also, the uncertainty in the total cross section at the LHC increases as m_{A^0} increases.

H. Differential cross sections

Figure 19 shows the differential cross section as a function of the transverse momentum p_T of Z^0 and A^0 in the associated production of the $A^0 Z^0$ pairs at the LHC. We find that the NLO QCD correction could change the shape of transverse momentum distribution. The NLO QCD correction enhances the LO differential cross section in the low and the high p_T region, but reduces in the medium p_T region.

Figure 20 shows the differential cross section as a function of the invariant mass $M_{A^0 Z^0}$ of the $A^0 Z^0$ pairs produced at the LHC. The NLO QCD corrections reduce the LO differential cross sections more in the medium values of $M_{A^0 Z^0}$ and much less in low or high values of $M_{A^0 Z^0}$.

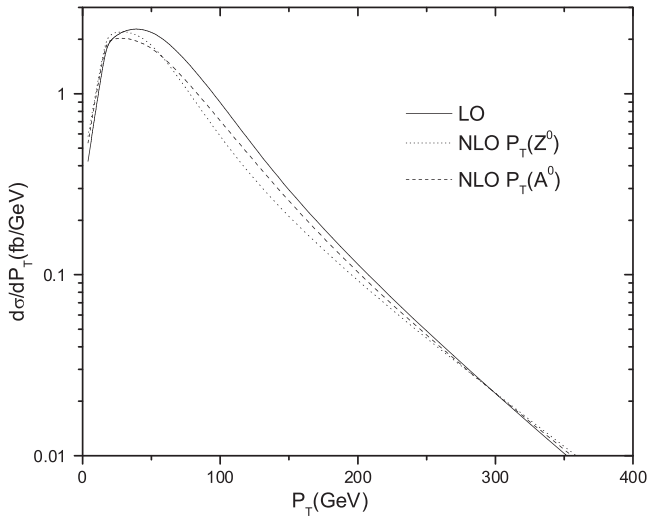

FIG. 19. Differential cross sections in the transverse momentum (p_T) of Z^0 and A^0 bosons, for the $A^0 Z^0$ production at the LHC, assuming: $m_0 = 200$ GeV, $m_{1/2} = 160$ GeV, $A_0 =$ 100 GeV, $\tan\beta = 40$, and $\mu < 0$.

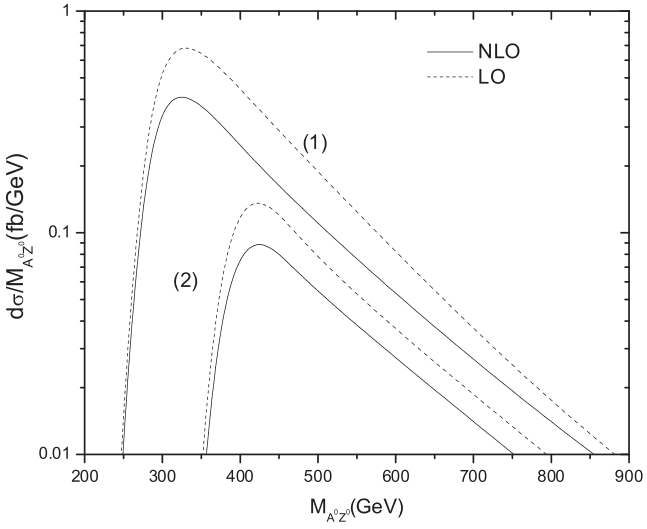

FIG. 20. Differential cross sections in the invariant mass ($M_{A^0 Z^0}$), for the $A^0 Z^0$ production at the LHC, assuming: (1) $m_0 = 200$ GeV, $m_{1/2} = 160$ GeV, $A_0 = 100$ GeV, $\tan\beta =$ 40, and $\mu < 0$; (2) $m_0 = 150$ GeV, $m_{1/2} = 180$ GeV, $A_0 =$ 300 GeV, $\tan\beta = 40$, and $\mu > 0$.

V. CONCLUSIONS

In conclusion, we have calculated the complete NLO QCD corrections to the inclusive total cross sections of the $A^0 Z^0$ pairs produced at the LHC in the MSSM. We have performed the calculations using both the DREG and the DRED schemes and found that the NLO total cross sections in the above two schemes are the same, which provides a cross-check to our calculations. Our results show that the LO total cross sections are a few tens fb in most of the SUSY parameter space and can exceed 100 fb for m_{A^0} below 160 GeV with large $\tan\beta$ ($\gtrsim 40$). The NLO correction can either enhance or reduce the total cross sections, but it generally efficiently reduces the dependence of the total cross sections on the renormalization/factorization scale. For small m_{A^0} and large $\tan\beta$, the K factor of SUSY-QCD corrections could become large, and using the QCD plus SUSY improved Yukawa coupling in the calculation could reduce the size of the overall K factor. We have also examined the uncertainty in total cross sections due to the PDF uncertainties and found that the uncertainty in NLO cross sections is slightly larger than that in LO ones, especially at large m_{A^0}. Finally, we also examined a few differential distributions and found that the NLO QCD corrections could change the shape of transverse momentum and invariant mass distributions.

ACKNOWLEDGMENTS

We thank Qing-Hong Cao and Tao Han for useful discussion. This work was supported in part by the National Natural Science Foundation of China and Specialized

Research Fund for the Doctoral Program of Higher Education. The work of C.-P. Y. was supported in part by the USA NSF Grant No. PHY-0244919.

APPENDIX A

In this appendix, we give the relevant Feynman rules.

(1) $h^0(H^0) - b - \bar{b}$: $A_{1(2)} m_b$

$$A_1 = \frac{igs_\alpha}{2m_w \cos\beta}, \qquad A_2 = \frac{-igc_\alpha}{2m_w \cos\beta},$$

where α is the mixing angle in the CP-even neutral Higgs boson sector [2]. Here we use the abbreviations $s_\alpha = \sin\alpha$ and $c_\alpha = \cos\alpha$.

(2) $A^0 - b - \bar{b}$: $A_3 m_b \gamma_5$

$$A_3 = \frac{-g\tan\beta}{2m_w}.$$

(3) $h^0(H^0) - Z^0 - A^0$: $F_{1(2)}(p_{h^0(H^0)} + p_{A^0})^\mu$

$$F_1 = \frac{g\cos(\beta-\alpha)}{2\cos\theta_w}, \qquad F_2 = \frac{-g\sin(\beta-\alpha)}{2\cos\theta_w}.$$

Here we define the outgoing four-momenta of $h^0(H^0)$ and A^0 to be negative and positive, respectively.

(4) $Z^0 - b - \bar{b}$: $\gamma_\mu(C_V + C_A\gamma_5)$

$$C_V = \frac{-ig}{2\cos\theta_w}\left(-\frac{1}{2} + \frac{2}{3}\sin^2\theta_w\right), \qquad C_A = \frac{-ig}{4\cos\theta_w}.$$

(5) $h^0(H^0, A^0) - \tilde{b}_\alpha - \tilde{b}_\beta$: $i[R^{\tilde{b}}\hat{G}^{\tilde{b}}_{1(2,3)}(R^{\tilde{b}})^T]_{\alpha\beta}$

$$\hat{G}^{\tilde{b}}_1 = \begin{pmatrix} \frac{gm_Z}{\cos\theta_w}(-\frac{1}{2} + \frac{1}{3}\sin\theta_w^2)\sin(\alpha+\beta) + \sqrt{2}m_b h_b s_\alpha & \frac{1}{\sqrt{2}}h_b[A_b s_\alpha + \mu c_\alpha] \\ \frac{1}{\sqrt{2}}h_b[A_b s_\alpha + \mu c_\alpha] & \frac{gm_Z}{\cos\theta_w}(-\frac{1}{3}\sin\theta_w^2)\sin(\alpha+\beta) + \sqrt{2}m_b h_b s_\alpha \end{pmatrix},$$

$$\hat{G}^{\tilde{b}}_2 = \begin{pmatrix} \frac{gm_Z}{\cos\theta_w}(\frac{1}{2} - \frac{1}{3}\sin\theta_w^2)\cos(\alpha+\beta) - \sqrt{2}m_b h_b c_\alpha & -\frac{1}{\sqrt{2}}h_b[A_b c_\alpha - \mu s_\alpha] \\ -\frac{1}{\sqrt{2}}h_b[A_b c_\alpha - \mu s_\alpha] & \frac{gm_Z}{\cos\theta_w}(\frac{1}{3}\sin\theta_w^2)\cos(\alpha+\beta) - \sqrt{2}m_b h_b c_\alpha \end{pmatrix},$$

$$\hat{G}^{\tilde{b}}_3 = i\frac{gm_b}{2m_W}\begin{pmatrix} 0 & -A_b\tan\beta - \mu \\ A_b\tan\beta + \mu & 0 \end{pmatrix},$$

with $h_b = gm_b/\sqrt{2}m_W\cos\beta$.

(6) $Z^0 - \tilde{b}_\alpha - \tilde{b}_\beta$: $(-ig/\cos\theta_w)T_Z(\alpha,\beta)(p_{\tilde{b}_\alpha} + p_{\tilde{b}_\beta})^\mu$

$$T_Z = \begin{pmatrix} -\frac{1}{2}\cos^2_{\theta_{\tilde{b}}} + \frac{1}{3}\sin^2_{\theta_w} & \frac{1}{4}\sin 2\theta_{\tilde{b}} \\ \frac{1}{4}\sin 2\theta_{\tilde{b}} & -\frac{1}{2}\sin^2_{\theta_{\tilde{b}}} + \frac{1}{3}\sin^2_{\theta_w} \end{pmatrix},$$

where $p_{\tilde{b}_\alpha}$ and $p_{\tilde{b}_\beta}$ are the four-momenta of $\tilde{b}_\alpha$ and $\tilde{b}_\beta$, respectively, in the direction of the charge flow.

APPENDIX B

In this appendix, we collect the explicit expressions of the nonzero form factors in Eqs. (14) and (15). Since $\overline{\sum} M^0 M^\dagger_{j=7,8,\ldots 12} = 0$, only the form factors of the first six matrix elements are presented here. For simplicity, we introduce the following abbreviations for the Passarino-Veltman three-point integrals $C_{i(j)}$ and four-point integrals $D_{i(j)}$, which are defined similarly to Ref. [26] except that we take internal masses squared as arguments:

$$C^a_{i(j)} = C_{i(j)}(0, 0, s, 0, 0, 0),$$

$$C^b_{i(j)} = C_{i(j)}(m^2_{A^0}, t, 0, 0, 0, 0),$$

$$C^c_{i(j)} = C_{i(j)}(m^2_Z, u, 0, 0, 0, 0),$$

$$C^d_{i(j)} = C_{i(j)}(m^2_{A^0}, 0, u, 0, 0, 0),$$

$$C^e_{i(j)} = C_{i(j)}(m^2_z, 0, t, 0, 0, 0),$$

$$C^f_{i(j)} = C_{i(j)}(t, 0, m^2_z, 0, 0, 0),$$

$$C^g_{i(j)} = C_{i(j)}(u, 0, m^2_z, 0, 0, 0),$$

$$C^h_{i(j)} = C_{i(j)}(u, 0, m^2_{A^0}, 0, 0, 0),$$

$$C^i_{i(j)} = C_{i(j)}(m^2_Z, t, 0, 0, 0, 0),$$

$$C^j_{i(j)} = C_{i(j)}(u, m^2_{A^0}, 0, 0, 0, 0),$$

$$C^k_{i(j)} = C_{i(j)}(m^2_{A^0}, t, 0, 0, 0, 0),$$

$$C^l_{i(j)} = C_{i(j)}(0, m^2_Z, u, 0, 0, 0),$$

$$C^u_{i(j)} = C_{i(j)}(s, 0, 0, 0, 0, 0),$$

$$C^v_{i(j)} = C_{i(j)}(0, u, m^2_Z, 0, 0, 0),$$

$$C^x_{i(j)} = C_{i(j)}(s, m^2_{A^0}, m^2_Z, 0, 0, 0),$$

$$C^{y}_{i(j)} = C_{i(j)}(0, m^2_{A^0}, t, 0, 0, 0),$$

$$C^{z}_{i(j)} = C_{i(j)}(0, t, m^2_Z, 0, 0, 0),$$

$$C^{m}_{i(j)}(a, b) = C_{i(j)}(0, 0, s, m^2_{\tilde{b}_a}, m^2_{\tilde{g}}, m^2_{\tilde{b}_b}),$$

$$C^{n}_{i(j)}(a, b) = C_{i(j)}(m^2_{A^0}, t, 0, m^2_{\tilde{b}_b}, m^2_{\tilde{b}_a}, m^2_{\tilde{g}}),$$

$$C^{o}_{i(j)}(a, b) = C_{i(j)}(0, u, m^2_Z, m^2_{\tilde{b}_b}, m^2_{\tilde{b}_a}, m^2_{\tilde{g}}),$$

$$C^{p}_{i(j)}(a, b) = C_{i(j)}(m^2_{A^0}, 0, u, m^2_{\tilde{b}_b}, m^2_{\tilde{b}_a}, m^2_{\tilde{g}}),$$

$$C^{q}_{i(j)}(a, b) = C_{i(j)}(t, m^2_Z, 0, m^2_{\tilde{g}}, m^2_{\tilde{b}_b}, m^2_{\tilde{b}_a}),$$

$$C^{r}_{i(j)}(a, b) = C_{i(j)}(u, 0, m^2_{A^0}, m^2_{\tilde{b}_b}, m^2_{\tilde{b}_a}, m^2_{\tilde{g}}),$$

$$C^{s}_{i(j)}(a, b) = C_{i(j)}(u, m^2_{A^0}, 0, m^2_{\tilde{g}}, m^2_{\tilde{b}_b}, m^2_{\tilde{b}_a}),$$

$$C^{t}_{i(j)}(a, b) = C_{i(j)}(0, m^2_{A^0}, t, m^2_{\tilde{g}}, m^2_{\tilde{b}_b}, m^2_{\tilde{b}_a}),$$

$$D^{a}_{i(j)} = D_{i(j)}(s, 0, t, m^2_{A^0}, 0, m^2_Z, 0, 0, 0, 0),$$

$$D^{b}_{i(j)} = D_{i(j)}(0, t, m^2_Z, s, m^2_{A^0}, 0, 0, 0, 0, 0),$$

$$D^{c}_{i(j)} = D_{i(j)}(s, 0, u, m^2_Z, 0, m^2_{A^0}, 0, 0, 0, 0),$$

$$D^{d}_{i(j)} = D_{i(j)}(0, u, m^2_{A^0}, s, m^2_z, 0, 0, 0, 0, 0),$$

$$D^{e}_{i(j)}(a, b, l) = D_{i(j)}(s, 0, t, m^2_{A^0}, 0, m^2_Z, m^2_{\tilde{b}_b}, m^2_{\tilde{b}_a}, m^2_{\tilde{g}}, m^2_{\tilde{b}_l}),$$

$$D^{f}_{i(j)}(a, b, l) = D_{i(j)}(0, 0, m^2_Z, m^2_{A^0}, s, t, m^2_{\tilde{b}_b}, m^2_{\tilde{g}}, m^2_{\tilde{b}_a}, m^2_{\tilde{b}_l}),$$

$$D^{h}_{i(j)}(a, b, l) = D_{i(j)}(s, 0, u, m^2_Z, 0, m^2_{A^0}, m^2_{\tilde{b}_b}, m^2_{\tilde{b}_a}, m^2_{\tilde{g}}, m^2_{\tilde{b}_l}).$$

Many of the above functions contain the soft and/or collinear singularities. Since all the Passarino-Veltman integrals can be written as a combination of the scalar functions A_0, B_0, C_0, and D_0, we present here the explicit expressions for the C_0 and D_0 functions used in our calculations:

$$C^a_0 = C^u_0 = \frac{C_\epsilon}{s}\left[\frac{1}{\epsilon^2} - \frac{\pi^2}{3}\right], \qquad C^d_0 = C^h_0 = C^j_0 = \frac{C_\epsilon}{u - m^2_{A^0}}\left[\frac{1}{\epsilon}\ln\left(\frac{-u}{m^2_{A^0}}\right) + \frac{1}{2}\ln^2\left(\frac{s}{m^2_{A^0}}\right) - \frac{1}{2}\ln^2\left(\frac{s}{-u}\right) - \frac{\pi^2}{2}\right],$$

$$C^c_0 = C^g_0 = C^l_0 = C^v_0 = \frac{C_\epsilon}{u - m^2_Z}\left[\frac{1}{\epsilon}\ln\left(\frac{-u}{m^2_Z}\right) + \frac{1}{2}\ln^2\left(\frac{s}{m^2_Z}\right) - \frac{1}{2}\ln^2\left(\frac{s}{-u}\right) - \frac{\pi^2}{2}\right],$$

$$C^e_0 = C^f_0 = C^i_0 = C^y_0 = \frac{C_\epsilon}{t - m^2_Z}\left[\frac{1}{\epsilon}\ln\left(\frac{-t}{m^2_Z}\right) + \frac{1}{2}\ln^2\left(\frac{s}{m^2_Z}\right) - \frac{1}{2}\ln^2\left(\frac{s}{-t}\right) - \frac{\pi^2}{2}\right],$$

$$C^b_0 = C^k_0 = C^x_0 = \frac{C_\epsilon}{t - m^2_{A^0}}\left[\frac{1}{\epsilon}\ln\left(\frac{-t}{m^2_{A^0}}\right) + \frac{1}{2}\ln^2\left(\frac{s}{m^2_{A^0}}\right) - \frac{1}{2}\ln^2\left(\frac{s}{-t}\right) - \frac{\pi^2}{2}\right],$$

$$\begin{aligned} D^a_0 = D^b_0 = {} & \frac{C_\epsilon}{st}\left[\frac{1}{\epsilon^2} + \frac{2}{\epsilon}\ln\left(\frac{m_Z m_{A^0}}{-t}\right) + \frac{\pi^2}{3}\right] - 2\frac{C_\epsilon}{st}\left\{\mathrm{Li}\left(\frac{m^2_{A^0} - u}{s}\right) - \mathrm{Li}\left(\frac{s - m^2_Z}{s}\right) - \mathrm{Li}\left[\frac{-st}{(s - m^2_Z)(m^2_Z - t)}\right]\right. \\ & + \mathrm{Li}\left(\frac{-t}{s - m^2_Z}\right) + \mathrm{Li}\left(\frac{m^2_{A^0}}{m^2_{A^0} - t}\right) - \frac{1}{2}\ln^2\left[\frac{-st}{(s - m^2_Z)(m^2_Z - t)}\right] + \frac{1}{2}\ln^2\left(\frac{-t}{s - m^2_Z}\right) + \ln\left(\frac{m^2_Z - t}{s}\right)\ln\left(\frac{m^2_{A^0} - u}{t}\right) \\ & \left. - \frac{1}{2}\ln\left(\frac{m^2_Z - t}{s}\right)\ln\left(\frac{s m^2_{A^0}}{t^2}\right) + \frac{1}{4}\ln^2\left(\frac{s m^2_{A^0}}{t^2}\right) + \frac{1}{4}\ln^2\left(\frac{m^2_Z}{s}\right) + \frac{1}{2}\ln\left(\frac{m^2_{A^0}}{s}\right)\ln\left(\frac{m^2_Z - t}{m^2_Z}\right) + \frac{1}{2}\ln^2\left(\frac{m^2_{A^0}}{m^2_{A^0} - t}\right)\right\}, \end{aligned}$$

$$D^c_0 = D^d_0 = D^a_0(t \leftrightarrow u, m^2_{A^0} \leftrightarrow m^2_Z),$$

where $C_\epsilon = (4\pi\mu_r^2/s)^\epsilon\Gamma(1 - \epsilon)/\Gamma(1 - 2\epsilon)$.

For diagrams (a)–(g) in Fig. 2, we get the form factors as following, respectively:

$$f_1^a = \frac{-4\alpha_s}{3\pi(s-m_{h_0}^2)(s-m_{H_0}^2)}\{ism_b[A_1F_1(s-m_{H_0}^2)+A_2F_2(s-m_{h_0}^2)]C_0^a + F_1m_{\tilde{g}}(s-m_{H_0}^2)\hat{G}_1^{\tilde{b}}(a,b)R_{a,1}^{\tilde{b}}R_{b,2}^{\tilde{b}}C_0^m$$
$$+ F_2m_{\tilde{g}}(s-m_{h_0}^2)\hat{G}_2^{\tilde{b}}(a,b)R_{a,1}^{\tilde{b}}R_{b,2}^{\tilde{b}}C_0^m\} + \frac{4\alpha_s\epsilon}{3\pi(s-m_{h_0}^2)(s-m_{H_0}^2)}[A_1F_1(s-m_{H_0}^2)+A_2F_2(s-m_{h_0}^2)]B_0(s,0,0),$$

$$f_2^a = f_1^a,$$

$$f_3^a = \frac{4m_{\tilde{g}}\alpha_s(R_{a,2}^{\tilde{b}}R_{b,1}^{\tilde{b}} - R_{a,1}^{\tilde{b}}R_{b,2}^{\tilde{b}})}{3\pi(s-m_{h_0}^2)(s-m_{H_0}^2)}[F_1\hat{G}_1^{\tilde{b}}(a,b)(s-m_{H_0}^2)+F_2\hat{G}_2^{\tilde{b}}(a,b)(s-m_{h_0}^2)]C_0^m,$$

$$f_4^a = f_3^a,$$

$$f_1^b = \frac{4im_bA_3(C_V-C_A)\alpha_s}{3\pi t}[(1-\epsilon)(2C_{00}^f - uC_{12}^f + (t-m_{A_0}^2)C_{11}^f + m_Z^2C_1^e - (s-m_Z^2-m_{A_0}^2)C_{12}^f + m_{A_0}^2C_{11}^f$$
$$- B_0(t,0,0)) + m_Z^2C_0^i + tC_1^f] - \frac{4m_bg\alpha_sA_3T_Z(a,b)R_{a1}^{\tilde{b}}R_{b1}^{\tilde{b}}}{3\pi t\cos\theta_w}[2c_{00}^q + uC_2^q + uC_{22}^q$$
$$+ (t-m_{A_0}^2)(C_1^q + C_{11}^q + C_2^q + C_{22}^q) + (s-m_Z^2-m_{A_0}^2)(C_2^q + C_{22}^q) + m_{A_0}^2(C_1^q + C_{11}^q + C_2^q + C_{22}^q) + tC_{12}^q],$$

$$f_3^b = \frac{-4im_bC_VA_3\alpha_s}{3\pi t}\{(1-\epsilon)[2C_{00}^f - uC_{12}^f + (t-m_{A_0}^2)C_{11}^f + m_Z^2C_1^e - (s-m_Z^2-m_{A_0}^2)C_{12}^f + m_{A_0}^2C_{11}^f - B_0(t,0,0)]$$
$$+ m_Z^2C_0^i + tC_1^f\} + \frac{4m_bg\alpha_sA_3T_Z(a,b)R_{a1}^{\tilde{b}}R_{b1}^{\tilde{b}}}{3\pi t\cos\theta_w}[2C_{00}^q + uC_2^q + uC_{22}^q + (t-m_{A_0}^2)(C_1^q + C_{11}^q + C_2^q + C_{22}^q)$$
$$+ (s-m_Z^2-m_{A_0}^2)(C_2^q + C_{22}^q) + m_{A_0}^2(C_1^q + C_{11}^q + C_2^q + C_{22}^q) + tC_{12}^q],$$

$$f_5^b = \frac{-2im_b\alpha_sA_3(C_V-C_A)}{3\pi t}\{(1-\epsilon)[2C_{00}^f + (t-m_{A_0}^2)C_1^f + m_Z^2C_1^e + (s-m_Z^2-m_{A_0}^2)(C_1^e - C_2^f) + m_{A_0}^2(2C_1^f - C_2^e)$$
$$- B_0(t,0,0)] + m_Z^2C_0^i\} + \frac{2gm_b\alpha_sA_3T_Z(ab)R_{a1}^{\tilde{b}}R_{b1}^{\tilde{b}}}{3\pi\cos\theta_w t}C_{00}^q,$$

$$f_6^b = \frac{4im_b\alpha_sC_VA_3}{3\pi t}\{(1-\epsilon)[2C_{00}^f + (t-m_{A_0}^2)C_1^f + m_Z^2C_1^e + (s-m_Z^2-m_{A_0}^2)(C_1^e - C_2^f) + m_{A_0}^2(2C_1^f - C_2^e) - B_0(t,0,0)]$$
$$+ m_Z^2C_0^i\} + \frac{-4gm_b\alpha_sA_3T_Z(a,b)R_{a1}^{\tilde{b}}R_{b1}^{\tilde{b}}}{3\pi\cos\theta_w t}C_{00}^q,$$

$$f_1^c = \epsilon\frac{-4im_bA_3\alpha_s}{3\pi}(C_V+C_A)(C_1^d - C_2^h),$$

$$f_2^c = \frac{-4im_bA_3\alpha_s}{3\pi u}(C_V+C_A)[m_{A_0}^2C_0^j - B_0(u,0,0)] + \frac{4m_{\tilde{g}}\alpha_s}{3\pi u}\hat{G}_3^{\tilde{b}}(a,b)R_{a1}^{\tilde{b}}R_{b2}^{\tilde{b}}C_0^s + \epsilon\frac{-4im_bA_3\alpha_s}{3\pi u}$$
$$\times(C_V+C_A)[uC_1^d + uC_2^d - uC_1^h - uC_2^h + (u-m_Z^2)C_1^h - m_Z^2(C_2^d - 2C_1^h) + (s-m_Z^2-m_{A^0}^2)(C_1^d - C_2^h)$$
$$+ m_{A^0}^2C_1^d + B_0(u,0,0)],$$

$$f_3^c = \epsilon\frac{8im_bA_3\alpha_s}{3\pi}C_V(C_1^d - C_2^h),$$

$$f_4^c = \frac{8im_bA_3\alpha_sC_V}{3\pi u}[m_{A_0}^2C_0^j - B_0(u,0,0)] + \frac{4m_{\tilde{g}}\hat{G}_3^{\tilde{b}}(a,b)\alpha_s}{3\pi u}[R_{a2}^{\tilde{b}}R_{b1}^{\tilde{b}}(C_V-C_A)C_0^s - R_{a1}^{\tilde{b}}R_{b2}^{\tilde{b}}(C_V+C_A)C_0^s]$$
$$+ \epsilon\frac{8im_bA_3\alpha_s}{3\pi u}C_V[uC_1^d + uC_2^d - uC_1^h - uC_2^h + (u-m_Z^2)C_1^h - m_Z^2(C_2^d - 2C_1^h) + (s-m_Z^2-m_{A^0}^2)(C_1^d - C_2^h)$$
$$+ m_{A^0}^2C_1^d + B_0(u,0,0)],$$

$$f_5^c = \frac{-2im_bA_3\alpha_s}{3\pi u}(C_V+C_A)[m_{A_0}^2C_0^j - B_0(u,0,0)] + \frac{4m_{\tilde{g}}\alpha_s}{3\pi u}\hat{G}_3^{\tilde{b}}(a,b)R_{a1}^{\tilde{b}}R_{b2}^{\tilde{b}}C_0^s + \epsilon\frac{-2im_bA_3\alpha_s}{3\pi u}(C_V+C_A)$$
$$\times[uC_1^h + (s-m_Z^2-m_{A^0}^2)(C_1^d - C_2^h) - m_Z^2C_2^d + m_{A^0}^2C_1^d + B_0(u,0,0)],$$

$$f_6^c = \frac{4im_bA_3\alpha_sC_V}{3\pi u}[m_{A_0}^2C_0^j - B_0(u,0,0)] + \frac{4m_{\tilde g}\hat G_3^{\tilde b}(a,b)\alpha_s}{3\pi u}[R_{a2}^{\tilde b}R_{b1}^{\tilde b}(C_V - C_A)C_0^s - R_{a1}^{\tilde b}R_{b2}^{\tilde b}(C_V + C_A)C_0^s]$$
$$+ \epsilon\frac{4im_bA_3\alpha_s}{3\pi u}C_V[uC_1^h + (s - m_Z^2 - m_{A^0}^2)(C_1^d - C_2^h) - m_Z^2C_2^d + m_{A^0}^2C_1^d + B_0(u,0,0)],$$

$$f_1^d = \frac{4i(C_V - C_A)m_bA_3\alpha_s}{3\pi t}[C_0^km_{A_0}^2 - B_0(t,0,0)] + \frac{-4(C_V - C_A)m_{\tilde g}\alpha_s\hat G_3^{\tilde b}(a,b)R_{a1}^{\tilde b}R_{b2}^{\tilde b}}{3\pi t}C_0^t$$
$$+ \epsilon\frac{4i(C_V - C_A)m_bA_3\alpha_s}{3\pi t}[C_1^bm_{A_0}^2 + B_0(t,0,0)],$$

$$f_3^d = \frac{-8iC_Vm_bA_3\alpha_s}{3\pi t}[C_0^km_{A_0}^2 - B_0(t,0,0)] + \frac{-4(C_V + C_A)m_{\tilde g}\alpha_s\hat G_3^{\tilde b}(a,b)R_{a2}^{\tilde b}R_{b1}^{\tilde b}}{3\pi t}C_0^t$$
$$+ \frac{4(C_A - C_V)m_{\tilde g}\alpha_s\hat G_3^{\tilde b}(a,b)R_{a1}^{\tilde b}R_{b2}^{\tilde b}}{3\pi t}C_0^t + \epsilon\frac{-8iC_Vm_bA_3\alpha_s}{3\pi t}[C_1^bm_{A_0}^2 + B_0(t,0,0)],$$

$$f_5^d = \frac{-f_1^d}{2}, \qquad f_6^d = \frac{-f_3^d}{2},$$

$$f_2^e = \frac{-4i(C_V + C_A)m_bA_3\alpha_s}{3\pi u}[2C_{00}^g + uC_{11}^g + uC_{12}^g + m_Z^2(C_1^c + C_0^l)] + \frac{4gm_bA_3\alpha_s}{3\pi u\cos\theta_w}T_Z(a,b)R_{a2}^{\tilde b}R_{b2}^{\tilde b}(2C_{00}^o - uC_{12}^o),$$

$$f_4^e = \frac{8iC_Vm_bA_3\alpha_s}{3\pi u}[2C_{00}^g + uC_{11}^g + uC_{12}^g + m_Z^2(C_1^c + C_0^l)] + \frac{-4gm_bA_3\alpha_s}{3\pi u\cos\theta_w}T_Z(a,b)(2C_{00}^o - uC_{12}^o)(R_{a1}^{\tilde b}R_{b1}^{\tilde b} + R_{a2}^{\tilde b}R_{b2}^{\tilde b}),$$

$$f_5^e = \frac{-2i(C_V + C_A)m_bA_3\alpha_s}{3\pi u}[2C_{00}^g + uC_{11}^g + uC_{12}^g + m_Z^2(C_1^c + C_0^l)] + \frac{4gm_bA_3\alpha_s}{3\pi u\cos\theta_w}T_Z(a,b)R_{a2}^{\tilde b}R_{b2}^{\tilde b}C_{00}^o,$$

$$f_6^e = \frac{4iC_Vm_bA_3\alpha_s}{3\pi u}[2C_{00}^g + m_Z^2(C_1^c + C_0^l)] + \frac{-4gm_bA_3\alpha_s}{3\pi u\cos\theta_w}T_Z(a,b)C_{00}^o(R_{a1}^{\tilde b}R_{b1}^{\tilde b} + R_{a2}^{\tilde b}R_{b2}^{\tilde b}),$$

$$f_1^f = \frac{2i(C_V - C_A)m_bA_3\alpha_s}{3\pi t^2}R_{a1}^{\tilde b2}[-2m_{\tilde g}^2B_0(0,m_{\tilde g}^2,m_{\tilde g}^2) + m_{\tilde g}^2B_0(t,m_{\tilde g}^2,m_{\tilde b_a}^2) - 2m_{\tilde g}^2 + 2m_{\tilde b_a}^2B_0(0,m_{\tilde b_a}^2,m_{\tilde b_a}^2)$$
$$- m_{\tilde b_a}^2B_0(t,m_{\tilde g}^2,m_{\tilde b_a}^2) - 2m_{\tilde b_a}^2 + tB_0(t,m_{\tilde g}^2,m_{\tilde b_a}^2) + 2m_{\tilde b_a}^2B_0(0,m_{\tilde g}^2,m_{\tilde b_a}^2)] + \frac{2i(C_V - C_A)m_bA_3\alpha_s}{3\pi t^2}(1-\epsilon)tB_0(t,0,0),$$

$$f_3^f = \frac{-2im_bA_3\alpha_s}{3\pi t^2}[(C_V - C_A)R_{a1}^{\tilde b2} + (C_V + C_A)R_{a2}^{\tilde b2}][-2m_{\tilde g}^2B_0(0,m_{\tilde g}^2,m_{\tilde g}^2) + m_{\tilde g}^2B_0(t,m_{\tilde g}^2,m_{\tilde b_a}^2) + 2m_{\tilde b_a}^2B_0(0,m_{\tilde b_a}^2,m_{\tilde b_a}^2)$$
$$- 2m_{\tilde g}^2 - m_{\tilde b_a}^2B_0(t,m_{\tilde g}^2,m_{\tilde b_a}^2) - 2m_{\tilde b_a}^2 + tB_0(t,m_{\tilde g}^2,m_{\tilde b_a}^2) + 2m_{\tilde b_a}^2B_0(0,m_{\tilde g}^2,m_{\tilde b_a}^2)]$$
$$+ \frac{-2im_bA_3C_V\alpha_s}{3\pi t^2}(1-\epsilon)tB_0(t,0,0),$$

$$f_2^g = \frac{-2i(C_V + C_A)m_bA_3\alpha_s}{3\pi t^2}R_{a2}^{\tilde b2}[-2m_{\tilde g}^2B_0(0,m_{\tilde g}^2,m_{\tilde g}^2) + m_{\tilde g}^2B_0(t,m_{\tilde g}^2,m_{\tilde b_a}^2) + 2m_{\tilde b_a}^2B_0(0,m_{\tilde b_a}^2,m_{\tilde b_a}^2) - 2m_{\tilde g}^2$$
$$- m_{\tilde b_a}^2B_0(u,m_{\tilde g}^2,m_{\tilde b_a}^2) - 2m_{\tilde b_a}^2 + uB_0(u,m_{\tilde g}^2,m_{\tilde b_a}^2) + 2m_{\tilde b_a}^2B_0(0,m_{\tilde g}^2,m_{\tilde b_a}^2)]$$
$$+ \frac{-2i(C_V + C_A)m_bA_3\alpha_s}{3\pi t^2}(1-\epsilon)uB_0(u,0,0),$$

$$f_4^g = \frac{2im_bA_3\alpha_s}{3\pi u^2}[(C_V - C_A)R_{a1}^{\tilde b2} + (C_V + C_A)R_{a2}^{\tilde b2}][-2m_{\tilde g}^2B_0(0,m_{\tilde g}^2,m_{\tilde g}^2) + m_{\tilde g}^2B_0(u,m_{\tilde g}^2,m_{\tilde b_a}^2) + 2m_{\tilde b_a}^2B_0(0,m_{\tilde b_a}^2,m_{\tilde b_a}^2)$$
$$- 2m_{\tilde g}^2 - m_{\tilde b_a}^2B_0(u,m_{\tilde g}^2,m_{\tilde b_a}^2) - 2m_{\tilde b_a}^2 + uB_0(u,m_{\tilde g}^2,m_{\tilde b_a}^2) + 2m_{\tilde b_a}^2B_0(0,m_{\tilde g}^2,m_{\tilde b_a}^2)]$$
$$+ \frac{2im_bA_3C_V\alpha_s}{3\pi u^2}(1-\epsilon)uB_0(u,0,0),$$

$$f_5^g = \frac{-f_4^g}{2}, \qquad f_6^f = \frac{-f_2^g}{2}.$$

For the box diagrams (a)–(d) in Fig. 3, we find, respectively,

$$f_1^{\mathrm{Box}(a)} = \frac{-4im_bA_3(C_V - C_A)\alpha_s}{3\pi}[-C_2^e - sD_0^a + uD_2^b - (t - m_{A^0}^2)(D_2^b + D_3^b - D_1^a - D_3^a) + (1+\epsilon)(C_0^y - C_0^x)]$$
$$+ \epsilon\frac{-4im_bA_3(C_V - C_A)\alpha_s}{3\pi}[C_2^e + C_1^u + (u - m_{A^0}^2)(D_{11}^a + D_{13}^a) - (t - m_{A^0}^2)(D_2^b + D_3^b)$$
$$- m_{A^0}^2(D_1^a + D_{13}^a + D_3^a + D_{33}^a)],$$

$$f_2^{\mathrm{Box}(a)} = \frac{4im_bA_3(C_V - C_A)\alpha_s}{3\pi}[m_{A^0}^2(D_0^a + D_2^b) - (t - m_{A^0}^2)(D_1^a + D_2^a + D_3^a) - (u - m_{A^0}^2)D_3^b - C_0^a + C_0^z - C_0^x]$$
$$+ \epsilon\frac{4im_bA_3(C_V - C_A)\alpha_s}{3\pi}[2D_{00}^a - (u - m_{A^0}^2)(D_{11}^a + D_{12}^a + D_{13}^a + D_3^b) + m_{A^0}^2(D_{13}^a + D_{23}^a + D_{33}^a + D_2^b)],$$

$$f_3^{\mathrm{Box}(a)} = \frac{-2C_Vf_1^{\mathrm{Box}(a)}}{C_V - C_A}, \qquad f_4^{\mathrm{Box}(a)} = \frac{-2C_Vf_2^{\mathrm{Box}(a)}}{C_V - C_A},$$

$$f_5^{\mathrm{Box}(a)} = \frac{2im_bA_3(C_V - C_A)\alpha_s}{3\pi}[-sD_0^a + (u-t)D_0^a + C_0^y + C_0^z - 2C_0^x] + \epsilon\frac{2im_bA_3(C_V - C_A)\alpha_s}{3\pi}$$
$$\times[2D_{00}^a - (t - m_{A^0}^2)D_2^b - m_{A^0}^2D_3^a - C_0^x],$$

$$f_6^{\mathrm{Box}(a)} = \frac{-2C_Vf_5^{\mathrm{Box}(a)}}{C_V - C_A}, \qquad f_1^{\mathrm{Box}(b)} = \frac{4igm_{\tilde{g}}\alpha_s}{3\pi\cos\theta_w\cos\theta_w}T_Z(l,a)\hat{G}_3^{\tilde{b}}(l,b)R_{a1}^{\tilde{b}}R_{b2}^{\tilde{b}}(D_1^e + D_3^e + D_0^f),$$

$$f_2^{\mathrm{Box}(b)} = \frac{4igm_{\tilde{g}}\alpha_s}{3\pi\cos\theta_w\cos\theta_w}T_Z(l,a)\hat{G}_3^{\tilde{b}}(l,b)R_{a1}^{\tilde{b}}R_{b2}^{\tilde{b}}(D_1^e + D_2^e + D_3^e + D_0^f),$$

$$f_3^{\mathrm{Box}(b)} = \frac{4igm_{\tilde{g}}\alpha_s}{3\pi\cos\theta_w\cos\theta_w}T_Z(l,a)\hat{G}_3^{\tilde{b}}(l,b)(R_{b1}^{\tilde{b}} - R_{a1}^{\tilde{b}}R_{b2}^{\tilde{b}})(D_1^e + D_3^e + D_0^f),$$

$$f_4^{\mathrm{Box}(b)} = \frac{4igm_{\tilde{g}}\alpha_s}{3\pi\cos\theta_w\cos\theta_w}T_Z(l,a)\hat{G}_3^{\tilde{b}}(l,b)(R_{b1}^{\tilde{b}} - R_{a1}^{\tilde{b}}R_{b2}^{\tilde{b}})(D_1^e + D_2^e + D_3^e + D_0^f),$$

$$f_1^{\mathrm{Box}(c)} = \frac{-4im_bA_3(C_V + C_A)\alpha_s}{3\pi}[-sD_1^c + (u - m_Z^2)(D_3^d - D_1^c) - m_Z^2D_2^d - C_0^v]$$
$$+ \epsilon\frac{-4im_bA_3(C_V + C_A)\alpha_s}{3\pi}[C_1^d - C_1^u - C_1^x - (t - m_Z^2)D_{11}^c + (u - m_Z^2)D_3^d + m_Z^2(D_1^c + D_{13}^c)],$$

$$f_2^{\mathrm{Box}(c)} = \frac{-4im_bA_3(C_V + C_A)\alpha_s}{3\pi}[C_1^v - sD_1^c - sD_2^c - (t - m_Z^2)D_3^d - (u - m_Z^2)(D_1^c + D_2^c) + m_Z^2(D_0^c + D_2^d) - C_0^a]$$
$$+ \epsilon\frac{-4im_bA_3(C_V + C_A)\alpha_s}{3\pi}[C_1^d + C_2^d - C_1^x - (t - m_Z^2)(D_{11}^c + D_{12}^c + D_3^d) + m_Z^2(D_{13}^c + D_{23}^c + D_2^d) + C_0^v],$$

$$f_3^{\mathrm{Box}(c)} = \frac{-2C_Vf_1^{\mathrm{Box}(b)}}{C_V + C_A}, \qquad f_4^{\mathrm{Box}(c)} = \frac{-2C_Vf_2^{\mathrm{Box}(b)}}{C_V + C_A},$$

$$f_5^{\mathrm{Box}(c)} = \frac{2im_bA_3(C_V + C_A)\alpha_s}{3\pi}[-sD_0^c + (t-u)D_2^d + C_0^l + C_0^v - 2C_0^x] + \epsilon\frac{2im_bA_3(C_V + C_A)\alpha_s}{3\pi}$$
$$\times[2D_{00}^c - (u - m_{A^0}^2)D_2^d - m_Z^2D_3^c - C_0^x],$$

$$f_6^{\mathrm{Box}(c)} = \frac{-2C_Vf_5^{\mathrm{Box}(b)}}{C_V + C_A}, \qquad f_1^{\mathrm{Box}(d)} = \frac{4igm_{\tilde{g}}\alpha_s}{3\pi\cos\theta_w\cos\theta_w}T_Z(l,a)\hat{G}_3^{\tilde{b}}(l,b)R_{a1}^{\tilde{b}}R_{b2}^{\tilde{b}}D_1^h,$$

$$f_2^{\mathrm{Box}(d)} = \frac{4igm_{\tilde{g}}\alpha_s}{3\pi\cos\theta_w\cos\theta_w}T_Z(l,a)\hat{G}_3^{\tilde{b}}(l,b)R_{a1}^{\tilde{b}}R_{b2}^{\tilde{b}}(D_1^h + D_2^h),$$

$$f_3^{\mathrm{Box}(d)} = \frac{4igm_{\tilde{g}}\alpha_s}{3\pi\cos\theta_w\cos\theta_w}T_Z(l,a)\hat{G}_3^{\tilde{b}}(l,b)(R_{b1}^{\tilde{b}} - R_{a1}^{\tilde{b}}R_{b2}^{\tilde{b}})D_1^h,$$

$$f_4^{\mathrm{Box}(b)} = \frac{4igm_{\tilde{g}}\alpha_s}{3\pi\cos\theta_w}T_Z(l,a)\hat{G}_3^{\tilde{b}}(l,b)(R_{a2}^{\tilde{b}}R_{b1}^{\tilde{b}} - R_{a1}^{\tilde{b}}R_{b2}^{\tilde{b}})(D_1^h + D_2^h).$$

[1] T. Hambye and K. Riesselmann, Phys. Rev. D **55**, 7255 (1997).
[2] H. E. Haber and G. L. Kane, Phys. Rep. **117**, 75 (1985).
[3] H. E. Haber and R. Hempfling, Phys. Rev. Lett. **66**, 1815 (1991); Y. Okada *et al.*, Prog. Theor. Phys. **85**, 1 (1991); J. Ellis *et al.*, Phys. Lett. B **257**, 83 (1991); S. Heinemeyer, hep-ph/0407244.
[4] A. Djouadi, Pramana **62**, 191 (2004); M. Dittmar, Pramana **55**, 151 (2000); F. Gianotti, CERN, 2000 (unpublished).
[5] F. Gianotti *et al.*, Eur. Phys. J. C **39**, 293 (2005); D. Denegri *et al.*, hep-ph/0112045.
[6] H. Georgi *et al.*, Phys. Rev. Lett. **40**, 692 (1978).
[7] M. Spira *et al.*, Phys. Lett. B **318**, 347 (1993); Nucl. Phys. **B453**, 17 (1995); S. Dawson *et al.*, Phys. Rev. Lett. **77**, 16 (1996); Robert V. Harlander and Matthias Steinhauser, Phys. Lett. B **574**, 258 (2003); Phys. Rev. D **68**, 111701 (2003); J. High Energy Phys. 09 (2004) 066; A. Djouadi and M. Spira, Phys. Rev. D **62**, 014004 (2000).
[8] R. V. Harlander and W. Kilgore, Phys. Rev. Lett. **88**, 201801 (2002); J. High Energy Phys. 10 (2002) 017; C. Anastasiou and K. Melnikov, Nucl. Phys. **B646**, 220 (2002); Phys. Rev. D **67**, 037501 (2003); V. Ravindran *et al.*, Nucl. Phys. **B665**, 325 (2003).
[9] S. Catani *et al.*, J. High Energy Phys. 07 (2003) 028; A. Kulesza *et al.*, Phys. Rev. D **69**, 014012 (2004).
[10] R. N. Cahn and S. Dawson, Phys. Lett. **136B**, 196 (1984); G. Altarelli *et al.*, Nucl. Phys. **B287**, 205 (1987); T. Han *et al.*, Phys. Rev. Lett. **69**, 3274 (1992).
[11] S. Glashow *et al.*, Phys. Rev. D **18**, 1724 (1978).
[12] R. Kleiss, Z. Kunszt, and W. J. Stirling, Phys. Lett. B **253**, 269 (1991).
[13] T. Han and S. Willenbrock, Phys. Lett. B **273**, 167 (1991).
[14] Z. Kunszt, Nucl. Phys. **B247**, 339 (1984); W. Beenakker *et al.*, Phys. Rev. Lett. **87**, 201805 (2001); Nucl. Phys. **B653**, 151 (2003); S. Dawson *et al.*, Phys. Rev. Lett. **87**, 201804 (2001); Phys. Rev. D **67**, 071503 (2003); C. Balazs *et al.*, Phys. Rev. D **59**, 055016 (1999).
[15] A. A. Barrientos Bendezú and B. A. Kniehl, Phys. Rev. D **64**, 035006 (2001).
[16] J. Ohnemus *et al.*, Phys. Rev. D **47**, 2722 (1993); H. Baer *et al.*, Phys. Rev. D **47**, 2730 (1993).
[17] L. L. Yang *et al.*, J. Phys. G **30**, 1821 (2004).
[18] Y. Jun *et al.*, Phys. Rev. D **66**, 095008 (2002).
[19] Chung Kao and Shankar Sachithanandam, Phys. Lett. B **620**, 80 (2005).
[20] Chung Kao, Phys. Rev. D **46**, 4907 (1992).
[21] M. A. Aivazis *et al.*, Phys. Rev. D **50**, 3102 (1994); J. C. Collins, Phys. Rev. D **58**, 094002 (1998); M. Krämer *et al.*, Phys. Rev. D **62**, 096007 (2000).
[22] G. 't Hooft and M. J. G. Veltman, Nucl. Phys. **B44**, 189 (1972).
[23] M. Chanowitz *et al.*, Nucl. Phys. **B159**, 225 (1979).
[24] Z. Bern *et al.*, Phys. Rev. D **66**, 085002 (2002).
[25] A. Sirlin, Phys. Rev. D **22**, 971 (1980); W. J. Marciano and A. Sirlin, Phys. Rev. D **22**, 2695 (1980); **31**, 213(E) (1985); A. Sirlin and W. J. Marciano, Nucl. Phys. **B189**, 442 (1981); K. I. Aoki *et al.*, Prog. Theor. Phys. Suppl. **73**, 1 (1982).
[26] A. Denner, Fortschr. Phys. **41**, 307 (1993).
[27] S. Kraml, hep-ph/9903257; J. Ellis and S. Rudaz, Phys. Lett. **128B**, 248 (1983).
[28] G. Altarelli *et al.*, Nucl. Phys. **B157**, 461 (1979); J. C. Collins *et al.*, in *Perturbative Quantum Chromodynamics*, edited by A. H. Mueller (World Scientific, Singapore, 1989).
[29] B. W. Harris and J. F. Owens, Phys. Rev. D **65**, 094032 (2002).
[30] G. P. Lepage, J. Comput. Phys. **27**, 192 (1978).
[31] J. C. Collins *et al.*, Nucl. Phys. **B261**, 104 (1985); G. T. Bodwin, Phys. Rev. D **31**, 2616 (1985); **34**, 3932(E) (1986).
[32] G. Altarelli and G. Parisi, Nucl. Phys. **B126**, 298 (1977).
[33] R. K. Ellis *et al.*, Nucl. Phys. **B178**, 421 (1981); L. J. Bergmann, Ph.D. thesis, Florida State University, 1989; Z. Kunszt and D. E. Soper, Phys. Rev. D **46**, 192 (1992); M. L. Mangano *et al.*, Nucl. Phys. **B373**, 295 (1992).
[34] B. Kamal, Phys. Rev. D **53**, 1142 (1996).
[35] W. Beenakker *et al.*, Nucl. Phys. **B492**, 51 (1997).
[36] S. Eidelman *et al.* (Particle Data Group), Phys. Lett. B **592**, 1 (2004).
[37] S. G. Gorishny *et al.*, Mod. Phys. Lett. A **5**, 2703 (1990); Phys. Rev. D **43**, 1633 (1991); A. Djouadi *et al.*, Z. Phys. C **70**, 427 (1996); Comput. Phys. Commun. **108**, 56 (1998); M. Spira, Fortschr. Phys. **46**, 203 (1998).
[38] J. Pumplin *et al.*, J. High Energy Phys. 07 (2002) 012.
[39] M. Carena *et al.*, Nucl. Phys. **B577**, 88 (2000).
[40] M. Drees and S. P. Martin, hep-ph/9504324.
[41] A. Djouadi *et al.*, hep-ph/0211331.
[42] B. C. Allanach *et al.*, J. High Energy Phys. 09 (2004) 044.
[43] Howard E. Haber *et al.*, Phys. Rev. D **63**, 055004 (2001).
[44] D. Stump *et al.*, J. High Energy Phys. 10 (2003) 046.
[45] J. Pumplin *et al.*, J. High Energy Phys. 07 (2002) 012.